Technical Report
to the
Facility Impact and Financing Committee

J-PARC E06 Experiment

Measurement of T-violating Transverse Muon Polarization in $K \to \pi^0 \mu^+ \nu$ Decays

E06 (TREK) Collaboration*

June 4, 2007

*TREK is the acronym of "Time Reversal Experiment with Kaons". Group members are listed in Table 19; Contact person : J. Imazato (jun.imazato@kek.jp)

Contents

1 E06 (TREK) Experiment

The E06 (TREK) experiment is searching for T-violating transverse muon polarization (P_T) in the $K^+ \to \pi^0\mu^+\nu$ decay as a direct measure of T-violation. The time reversal (T) symmetry plays a unique role in particle physics. As a member of the triad of C, P, and T operations, T-invariance has implications for the other symmetries connecting the particle-antiparticle world and the mirror world. A discovery of a breakdown of T invariance implies CP violation if CPT symmetry holds. In particular, P_T is not induced in the Standard Model with the Kobayashi-Maskawa scheme, and hence it is very sensitive to any CP violation due to new physics. As a semi-leptonic process, it is sensitive to interference terms involving hadronic and leptonic currents and also exotic leptonic scalar interactions. Thus, P_T spans a complex scalar coupling phase space inaccessible for other phenomena [1].

This proposal is a sequel to the KEK-PS-E246 experiment. The full details and final results of the E246 experiment have recently been published [2]. The E246 experimental result constitutes the most precise estimate of the T-violation parameter, setting one of the most stringent constraints on scalar interactions. As remarked in this paper [2] this experiment also constrained the parameter spaces of scalar coupling in several models tighter than the present day results from B decays, or neutron EDM *etc.*

The E06 (TREK) experiment at J-PARC aims to improve our E246 result by a factor of 20. This goal is set, due to its physics significance and after considerations of the anticipated beam quality and intensity, the improved performance of the upgraded E246 detector assembly with present-day technology for the detector elements, electronics and data acquisitions. Unlike the case in E246, which was statistics limited, E06 (TREK) will push the measurement to the systematic limit. Also, E06 (TREK) will improve upon the systematics of E246 with detector assembly upgrades. Based on our vast experience with this decay channel and the measurement system of E246, we are convinced that our goal of pushing the limit $P_T < 2 \times 10^{-4}$ is attainable.

This report presents the details of the configuration of the E06 setup, the results of the measurements and simulations of the response of each component of the system along with the results of some R&Ds to this end. It should be emphasized that we already know the E246 system's response in great detail due to our vast experience with the system for the last 15 years. However, at the same time we realize that the improvement of the systematic errors by a factor of 10 will be a very hard task to be worked out intensively at the detector design stage. We are also very receptive to helpful criticisms of the outside people including the expert advice from the FIFC.

2 Detector Concept

2.1 E246 stopped-beam detector

The E06 (TREK) experiment will use the E246 setup at the KEK-PS by upgrading necessary detector parts. The most important feature of E246 was characterized by the use of stopped positive kaons. The E246 setup is based on a 12-gap superconducting toroidal magnet with a charged particle tracking system, an electromagnetic calorimeter and a muon polarimeter system. Details of the E246 setup were summarized in a technical paper [3] and its performance and the final result of the experiment was reported in [2]. The reasons for adopting the E246 upgraded detector in conjunction with the stopped beam method,

rather that a completely new detector at J-PARC were extensively outlined in the E06 proposal [1]. They are not repeated in this report, except for one essential argument that the performance and systematics of the detector (before upgrading) are thoroughly studied and well known. For a high-precision experiment the control of systematics is very important, and we can obtain a reliable prospect for the suppression of the systematic errors with the new detector after upgrading. The setup is shown in Fig.1.

Regarding the use of the stopped beam method, it is worth while to summarize its advantages briefly, since it is a prerequisite for adopting the E246 detector. The comparison between the stopped beam method and a conceivable in-flight decay method was critically discussed before in the BNL-AGS proposal E936 as well as in the present E06 proposal.

- Isotropic decay of K^+ at rest involves all the kinematic conditions covering the full decay phase space. By using a symmetric detector like E246, one can perform a double ratio measurement analyzing both regions of positive effect and negative effect with equal weight in the phase space.

- The energy range of decay particles extends only to about 250 MeV. It is rather easy to measure the particle energy in this range with high resolution. Decay particles are emitted in the entire 4π solid angle and CM angles can be measured with good accuracy with detector angular resolution.

- Due to the isotropic decay the event rates are distributed over highly-segmented detector elements. Thus, it is easy to design a system in which each detector element does not suffer from a high event rate. Also most parts of the detector can be located outside of the beam region.

- For a stopped beam experiment, one can start analysis from stopped kaons. The preceding characteristics of the beam such as beam emittance can be decoupled completely, which might otherwise bring about other systematics in the polarization measurement.

2.2 Principle of the experiment

In this experiment we are going to detect the muon transverse polarization, which is the spin polarization component normal to the decay plane, defined as

$$P_T = \frac{\vec{\sigma_\mu} \cdot (\vec{p}_{\pi^0} \times \vec{p}_{\mu^+})}{|\vec{p}_{\pi^0} \times \vec{p}_{\mu^+}|} \tag{1}$$

The pions are detected by the CsI(Tl) electromagnetic calorimeter as two photons and the muons are momentum-analyzed by the tracking system in the superconducting toroidal spectrometer. An event with a pion and a muon in relevant energy ranges is uniquely identified as a $K_{\mu 3}$ decay. Muon polarization is measured in the muon polarimeter by means of decay positron asymmetry. The direction (and the value) of P_T in the polarimeter is dependent on the kinematical region of π^0's reconstructed by CsI(Tl). For example, P_T lies in the azimuthal direction, namely clock-wise (cc) or counter-clock-wise (ccw) when pions are going in the forward (fwd) or backward (bwd) direction, respectively. By using

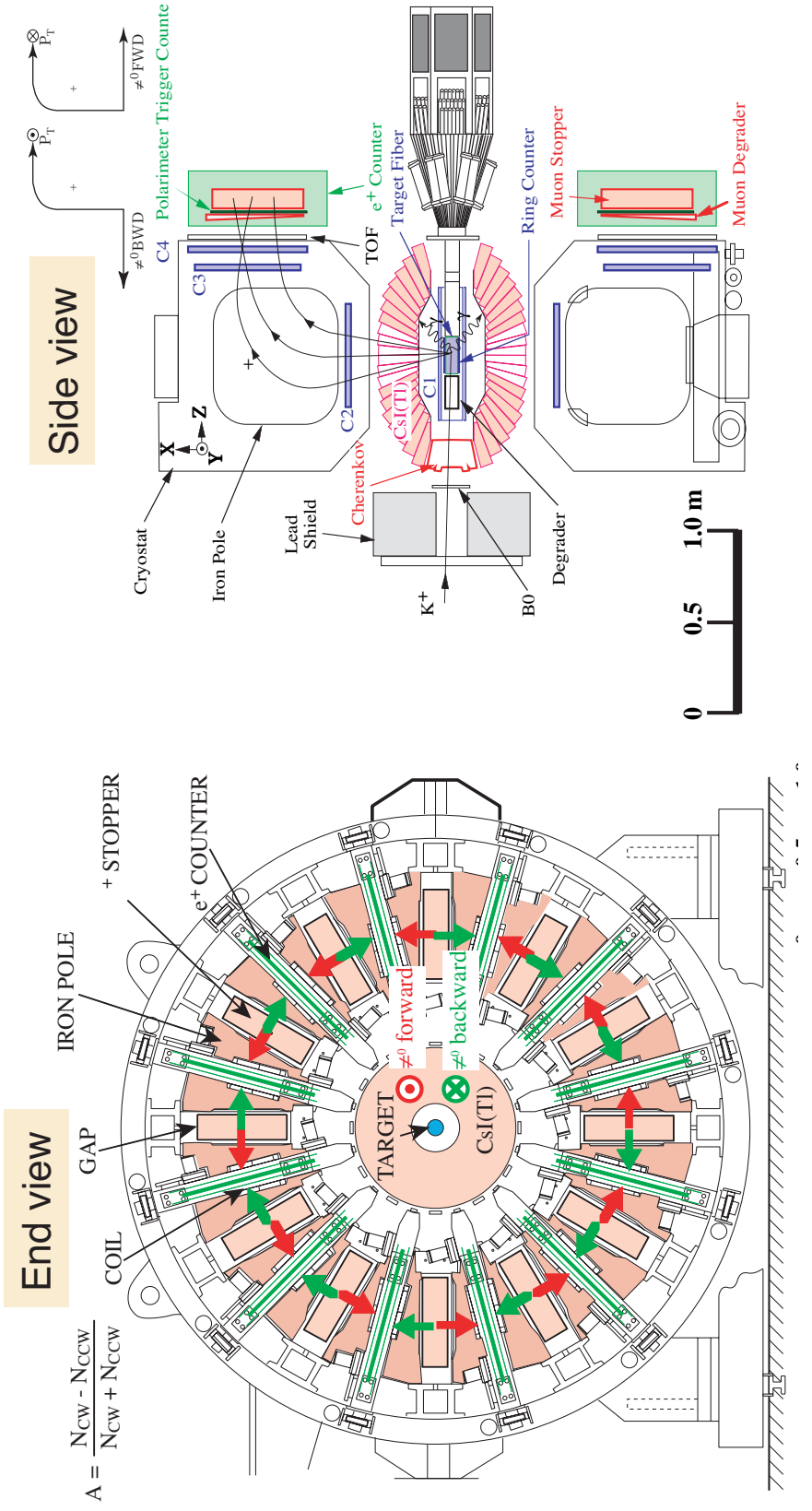

6

Figure 1: E246 setup

the so-called T-violating positron asymmetry (which is just the azimuthal asymmetry of positron emission in the poin fwd/bwd case) defined as

$$A_T = \frac{1}{2}(A_{fwd} - A_{bwd}), \tag{2}$$

and so-called analyzing power α and average kinematical attenuation factor $< \cos\theta_T >$, P_T in the most straightforward integrated analysis can be extracted as

$$< P_T >= \frac{A_T}{\alpha < \cos\theta_T >}. \tag{3}$$

In the proposal, other analysis possibilities for higher sensitivity were also discussed. We may use not only fwd/bwd regions of poins but also $left/right$ regions to analyze not azimuthal positron asymmetry but radial asymmetry. An event-by-event weighted analysis is also possible for any analyses. (See the proposal for details.)

2.3 Required rate performance of the detector

The E06 (TREK) experiment will be performed at K1.1-BR which will be installed at the T1 production target in the Phase-1 Hall. The beam optics have been designed as a short leg of the initially proposed K1.1 beamline branching after the first electrostatic separator and mass slit. The estimated positive kaon beam intensity at 800 MeV/c is 2×10^6/s at the primary proton intensity of 9 μA at 30 GeV from the J-PARC MR in Phase 1. This kaon beam intensity is 20 times higher than the intensity we had at K5 of KEK-PS. According to a realistic beam simulation we may expect a K^+/π^+ ratio better than one (about 3). Because we want to design TREK as the optimum experiment assuming this beam condition, we require that each detector element can work optimally for this kaon rate. Regarding pion contamination in the beam, which also contributes to singles rates in some detector elements such as the CsI(Tl) calorimeter, we cannot be too optimistic, but it would be a reasonable to assume a K^+/π^+ ratio of one. Upgraded elements are designed under these beam conditions and the other parts are also checked to operate at this beam intensity. Rate effect calculations starting from the E246 performance will be valid taking into account the difference of duty factor between 0.35 at K5 and 0.20 at K1.1-BR.

2.4 Systematic error suppression and experimental sensitivity

As mentioned above the goal of TREK is a sensitivity of 1×10^{-4} for P_T . This will be achieved by improving the statistical error by a factor 30 from E246 and suppressing the E246 systematic error by a factor of more than 10. A detailed estimate of the errors is given later. The development of the experiment from E246 to E06 (TREK) and beam conditions are summarized in Table 1.

2.5 Upgraded detector elements

The necessary upgrades have already been discussed in the proposal [1] in considerable detail. The major ones are (1) the active target, (2) charged particle tracking, (3) muon polarimeter, (4) muon magnetic field, (5) CsI(Tl) readout, and (6) readout electronics. The reasons for these upgrades are either (a) the improvement of rate performance, (b)

Table 1: Development from E246 to TREK and their beam conditions

Quantity	E246	E06 (TREK)
K^+ beam momentum	660 MeV/c	800 MeV/c
K^+ beam intensity	1.0×10^5/s	2×10^6/s
π/K ratio	~ 8	< 0.5
Duty factor	0.7 s/2.0 s = 0.35	0.7 s /3..5 s = 0.20
Net run time	1.8×10^7 s	1.4×10^7 s
Statistical error (σ)	2.3×10^{-3}	1×10^{-4}
Systematic error (σ)	1.1×10^{3}	$< 1 \times 10^4$
Total error (σ)	2.55×10^{-3}	$\sim 1.0 \times 10^{-4}$

Table 2: Detector upgrades and their reasons

Element	From E246 to E06 (TREK)	Reasons
Target	form 5 mm to 2.5 mm fiber smaller and lighter	(1) rate performance (2) better background rejection (3) suppression of systematic errors
Tracking	addition of C0 (and C1)	(1) rate performance (2) better background rejection
Polarimeter	passive to active	(1) acceptance improvement (2) analyzing power improvement (3) suppression of backgrounds (4) suppression of systematic errors
Muon filed	dedicated magnets	(1) improvement of analyzing power (2) suppression of systematic errors
CsI(Tl) readout	PIN to APD	(1) rate performance (2) better background rejection

the improvement of acceptance or polarization analyzing power, (c) better suppression of backgrounds, or (d) the suppression of systematic errors. They are summarized in Table 2. The overall comparison including the analysis method is shown in Table 3. Since the submission of the proposal more detailed design efforts have been continued and several basic performance checks were made. In the present report the updated designs will be shown item by item. The cost estimate is now more accurate based on the updated designs of the detector elements.

Table 3: Comparison of E06 (TREK) with E246

	This proposal	E246
Methodology		
Beam	stopped K^+	stopped K^+
Detector setup	Toroidal Spectrometer with upgraded E246 setup	Toroidal Spectrometer with E246 setup
Asymm. measurement		
Polarimeter	Active polarimeter	Passive polarimeter
Field method	Longitudinal $\mathbf{B} \parallel P_T$ $B = 300$ Gauss by dipole magnets	Longitudinal $<\mathbf{B}> \parallel P_T$ $B =$ 150-300 Gauss by SC toroidal magnet
π^0 selection	primarily in fwd and bwd integral or event-by-event, option of event by event in L/R $<\cos\theta_T>$ correction for integral	integral in fwd and bwd correction by $<\cos\theta_T>$
e^+ detection	event-by-event with E_{e^+}, θ_{e^+} measurement	integral in the e^+ counter
P_T deduction	integral analysis as E246 with weighted analysis option	use of analyzing power α $P_T = A_T/(\alpha <\cos\theta_T>)$
π^0 detection	2γ	$2\gamma + 1\gamma$
μ^+ tracking	4 (5) chambers + target	3 chambers + target
Alignment	10^{-4} by positioning and using data	10^{-3} by positioning
Main upgrades		
Tracking	C0(GEM)+(C1)+C2+C3+C4 in He gas bag	C2+C3+C4 in air
Target	$\sim$ 60mmϕ with 2.5 $\times$ 2.5mm Sci.fiber (L=0.2m) SiPMT readout	93mmϕ with 5 $\times$ 5mm Sci.fiber (L=1.85m) 1/2" PMT readout
π^0 detection	CsI(Tl) with APD readout with FADC	CsI(Tl) with PIN readout with PH-ADC
e^+ detection	active stopper with MWPCs	plastic counters
Data taking	KEK-VME, COPPER system	TKO+FASTBUS, UNIDAQ

3 Detector Upgrade

3.1 Muon polarimeter

3.1.1 Adoption of active polarimeter

The most important feature of the E06 (TREK) experiment is the adoption of an active polarimeter in contrast to E246 where a passive polarimeter with a separated system of a muon stopper and positron counter was used. Fig.2 shows a schematic view of the active polarimeter system. For the muon stopper, the parallel plates made of light metal (alloy) of Al or Mg are arranged in an orientation parallel to the spectrometer gap, namely parallel to the incident muon direction. A stopping efficiency higher than 0.95 can be obtained with the currently optimized parameters. A uniform muon field with large enough strength is applied parallel to the azimuthal direction to preserve the P_T component. A MWPC as a charged particle tracker is constructed with the plates as ground potential forming cells with a size of the plate gap (gap MWPC). In order not to put any disturbing materials in the muon incident path, the anode wires will be strung with 5mm pitch along the radial direction. Tracks due to muons and positrons are determined by connecting the hit positions of the gap MWPCs and their intersection point is treated as the muon stopped position. Thus, the decay vertices will be determined event-by-event. The current parameters of the stoppers and the gap MWPCs are summarized in Table 4.

Clearly, the present active polarimeter configuration is the best arrangement for the cw/ccw asymmetry measurement, as a single cell acts both as a cw cell and a ccw cell for the two neighboring plates. The channel inefficiency cancellation works perfectly. Since the active polarimeter determines the muon stopped position for each event, the systematic error associated with the ambiguity in the muon stopping distribution which is one of dominant contributions in the E246 experiment does not appear. Also, measurement of the positron energy determined by the range in the stopper materials and as well as is emission angle can improve the analyzing power of the asymmetry measurement. By requiring track consistency for positrons and muons, backgrounds can be drastically suppressed compared with the previous E246 experiment. Detection of decay positron in all the directions gives a polarimeter with a large acceptance with nearly 4π solid angle which is about 10 times larger than the E246 polarimeter system.

3.1.2 μSR study of muon stopper material

Among the polarimeter components, the muon stopper is an essential part of the present high precision polarization measurement of stopped muons. The spin polarization of incoming muons has to be preserved preferably without initial loss during stopping or relaxation, although such depolarizations affect only the sensitivity and they are not serious drawbacks to the experiment. Since the stopper plates function as the structure and also electrodes (ground) of the chamber to measure e^+'s, the requirements for the stopper material are:

- the material has to be a light element to suppress e^+ scattering and generation of showers.
- the plates have to have strong enough rigidity to be structural constituents. The material should also have a large yield strength.

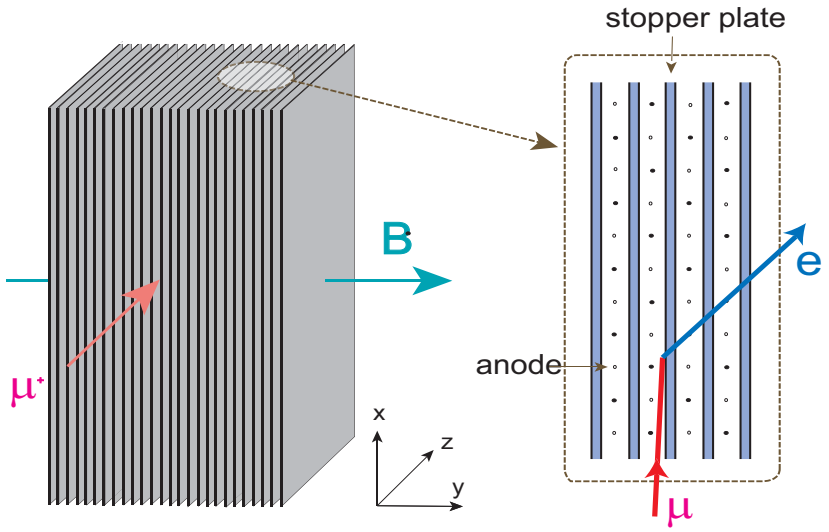

Figure 2: Schematic view of the active polarimeter system comprising muon stopper plates made of parallel plates and gap MWPCs. A cell structure is defined by two stopper plates and a MWPC between the plates. A single cell acts both as a *cw* cell and a *ccw* cell for the two neighboring plates and the channel inefficiency cancellation works perfectly.

Table 4: Main parameters of stopper and gap MWPC for the active polarimeter.

Stopper	
Number of plates	31
Material	Al, Mg or alloy
Thickness	typically 2 mm
Size	25 cm in z and 120 cm in r
Plate gap	typically 8 mm
Total number of incident particles	$\sim 10^4$/ sector
Gap MWPC	
Anode wire	20-μm-diameter Au-coated W
Anode pitch	5mm
Number of wires	$\sim$1200 per gap
Gas	Ar or He with buffer gas
Rate/wire	$\sim$ 300/s

- the surface of the plates serving as the ground electrodes have to kept clean for the long period of experiment without significant oxidation or erosion.

In previous experiments E246 and also E195 [4] which measured the $K_{\mu 2}$ polarization precisely, pure Al was used. However, this is not applicable to E06 because of its easy deformability. Contrary to the E246 stopper configuration the self-weight deformation might be problematic when the plates sit horizontally. If we want to use Al metal, some alloys might be better. Magnesium alloys are a quickly developing field. It is worth while to consider the magnesium alloys which are also lighter than Al. In order to test the muon depolarization characteristics for conceivable Al and Mg alloy candidates, we have recently (May '07) performed a μSR experiment at TRIUMF by using a dedicated short beam time (E1120) at the M20 channel to stop a surface muon beam with 100% polarization. By using the conventional LAMPF-OMNI spectrometer [5], transverse field (TF) as well as longitudinal field (LF) μSR measurements were carried out for the samples of Al and Mg alloys listed in Table 5[1]. Pure metals of Al and Mg were also measured as references. One of the typical TF asymmetry patterns for the magnesium alloy sample Z6 is shown in Fig. 3. Such a precession asymmetry pattern in the case of TF measurement was fitted to a asymmetry function with an exponential type relaxation and the relaxation rates were deduced. They are shown in Table 5. We found that almost all the tested samples except for one Al alloy (A2017) had small relaxation rates. In this experiment it was not intended to evaluate the initial polarization, but the asymmetry values are also shown in the table to give an idea. Because the E06 P_T measurement is primarily LF measurements, we performed LF for the test samples. The Front/Back asymmetry was fitted to an exponential type relaxation function. Since external LF acts as the decoupling field, the relaxation is suppressed. For all the samples we observed relaxation rates smaller than a few times $10^{-3}\mu\mathrm{s}^{-1}$. (Because the analysis of LF data is still going on, the results in the table are only preliminary with some unfitted parameters.) Thus, we confirmed that almost all the candidate materials of Al and Mg alloys are usable for the stopper from the point of view of muon spin behaviour. Now we have a number of choices to select the stopper from the other requirements.

3.1.3 Gap MWPC design

The basic cell structure consists of two stopper plates and a MWPC between the plates as shown in Fig. 2. The coordinate along the wire is determined by charge division on both ends. The angular determination of a positron track is done with the best condition for events in the $y-z$ plane. The positron into the radial direction r do not have good angular resolution, but it is sufficient for the present purpose. Although the muon field is applied in the azimuthal direction, e^+ tracks with relatively high momentum will be not affected.

The MWPCs are operated in proportional mode with Ar or He with buffer gas mixture. The signals from both ends of each wire are amplified in two stages. The first one is the preamplifier mounted on the polarimeter system which drives a cable going into the counting house where the signal is further amplified by the main amplifier. In order to reduce the number of channels, the signals from gap MWPC are summed up over all 12 sectors. Even in this case, an e^+ track can be easily identified by checking the consistency with a μ^+ track.

[1]The notation of alloys is a conventional way to indicate main admixed elements (in alphabet) with their concentrations in %.

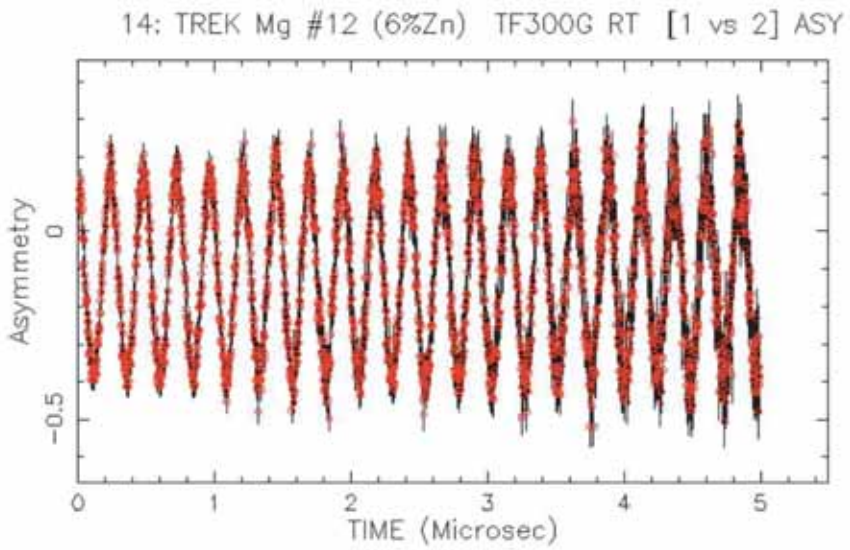

Figure 3: One of the typical TF asymmetry precession patterns measured at TRIUMF for a Mg alloy Z6 under the 0.03 T field. No relaxation was deduced in the fitting.

Table 5: Muon spin relaxation rate in TF and LF μSR measurements done at TRIUMF

	Sample	Asymmetry (%)	$\lambda^{TF}(\mu s^{-1})$	$\lambda^{LF}(\mu s^{-1})$
Al-alloy	pure Al annealed	28.3	0.00379 ± 0.00090	0.00044 ± 0.00071
	pure Al (99.55%)	28.5	0.00760 ± 0.00091	0.00027 ± 0.00075
	pure Al ($>$ 99.99%)	28.2	0.00338 ± 0.00087	0.00047 ± 0.00076
	A5052	28.2	0.01074 ± 0.00088	0.00066±???
	A6063	28.4	0.01564 ± 0.00090	0.00087 ± 0.00069
	A2017	29.2	0.04840 ± 0.00100	0.00021 ± 0.00067
Mg-alloy	pure Mg (99.95%)	27.8	0.00327 ± 0.00086	0.00166 ± 0.00072
	AZ31	28.0	0.00115 ± 0.00091	0.00000 ± 0.00020
	AZ31-PE	27.9	0.00041 ± 0.00092	0.00000 ± 0.00056
	ZK60	27.8	0.00030 ± 0.00111	0.00000 ± 0.00048
	Z6	27.9	0.00000 ± 0.00087	0.00079 ± 0.00072
	AM60	27.9	0.00000 ± 0.00043	0.00000 ± 0.00024
	AZ91	27.8	0.00270 ± 0.00093	0.00125 ± 0.00075

Analysis for LF measurements had not yet been completed and there are still ambiguity in the error evaluation.

Then, using a Q-T converter (QTC), the analogue signal is digitized to a logic pulse whose width is proportional to the analogue pulse height. There is no way to install a trigger counter for the positron measurement because it may produce an e^+ $left/right$ bias. This will be done by a muon incident trigger counter in front of the polarimeter and the positron time and charge measurement will be done over a long time range ($\sim$10 μs) using a high resolution ($\sim$1 ns) pipeline TDC with leading edge and trailing edge determinations.

3.1.4 Positron energy and angle measurements

The P_T asymmetry is a function of positron energy. Since low energy positrons have negative asymmetry they should be removed. In general an energy threshold E_e^{th} is set. Also, events with e^+ going to normal to the P_T direction dilute the asymmetry and should also be rejected. Thus, the e^+ selection with energy and emission angle is important to obtain the highest sensitivity for the P_T asymmetry measurement.

The positron energy is measured from the 'range' in the stopper materials. The magnetic analysis of the muon energy is rather difficult because the bending radius for a 35 MeV e^+ is $\sim$400 cm in a 0.03 T field and interaction with the stopper material introduces energy loss and scattering. Fig. 4 shows a density plot for the e^+ energy and the e^+ 'range' using Al plates. The 'range' was defined as the longest $e^{\pm}$ penetration depth also in the case of shower generation. Since a diagonal correlation is seen in the figure, we can set E_e^{th} in this figure. To achieve the highest analyzing power, a differential weighted analysis is also possible as was described in the proposal. In any analyses the positron energy thus determined by the 'range' has sufficiently good resolution. According to a Monte Carlo simulation, the FOM dependence on E_e^{th} is not very steep and e^+ discrimination by this method may keep the highest FOM level.

The e^+ emission angle is determined by the hit positions of the first and second gap MWPC and the angular resolution is thus modestly estimated. Assuming a 5mm wire pitch, the e^+ angular resolution is obtained to be 4.8° for E_{e^+} = 35 MeV and 4.7° for E_{e^+} = 50 MeV from the simulation. For high energy positrons, the angular resolution must be improved with the use of other MWPC information although the e^+ track will be distorted by the multiple scatterings in the plates. The FOM study by the simulation indicates the best threshold angle for the e^+ emission is $\theta_e^+ = 70°$ with respect to the azimuthal direction. Taking into account the e^+ angular resolution and the FOM structure, we can keep the high FOM level by rejecting events with e^+ tracks with less sensitivity to the P_T asymmetry.

3.2 Muon field magnet

3.2.1 Requirements

In the E06 upgraded detector, a new muon field magnet system will be installed. The reason for introducing the new magnets was discussed in the proposal. An external muon field is necessary for this high-precision polarization measurement in order to;

- to suppress spin relaxation in the stopper material, if any at zero-field, to preserve the experimental sensitivity,
- to decouple potential stray fields (including the earth's field) at the detector,

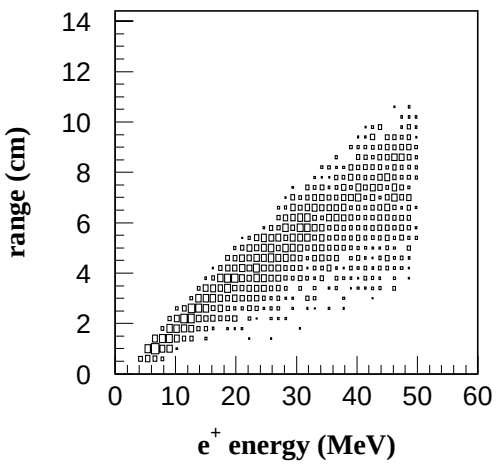

Figure 4: Scatter plot for the e^+ energy and the e^+ 'range' calculated in a MC stimulation for *Al* stoppers. The 'range' was defined as the longest $e^{\pm}$ penetration depth also in the case of shower generation. A diagonal correlation is seen,

- to enable positron energy analysis, eventually.

The third reason has less importance now, since we will obtain energy information primarily from the penetrating range. The magnetic analysis is rather difficult in the presence of scattering through the stopper plates, unless a fairly strong field is applied. The necessary field strength is determined to fulfill the other two requirements to be 0.03 T. This is one order of magnitude higher field than typical nuclear dipolar fields in materials. The μSR test experiment at TRIUMF also demonstrated that there should be no longitudinal field spin relaxation conceivable for the candidate stopper materials. Even if muon stopping in the chamber gas is finite and the muonium formation is significant at zero-field, the 0.03 T field brings back them to diamagnetic component almost totally [6].

Assuming a typical stray field of 0.3 Gauss in the experimental area, the 0.03 T external field decouples it to the $0.3/300 = 10^{-3}$ level. Even for an ideal geometrical alignment of the magnet, we have to regard this 10^{-3} as a misalignment potential of the field vector distribution. (In the actual case, the influence of stray fields in the magnet gaps is much smaller due to a shielding effect by the magnet poles.) Field mapping with the angular accuracy of $10^{-3} = 1$mr [7] will be performed and the field misalignment will be determined with this precision. As is discussed later, further alignment of the magnetic field distribution will be done by using real $K_{\mu 3}$ data with a precision of a few times of 10^{-4}. This alignment is preferable to ensure the accuracy for P_T, although its effect does not affect the accuracy of P_T.

Regarding the field strength and vector uniformities on the stopper, one has not to care too much, since we apply the field primarily for spin decoupling purpose. Only the

symmetric nature of the distribution becomes essential. A field uniformity of several percent will do, although our requirement in the proposal was rather strict and was a few %. When we analyze the pion L/R scheme with P_T in a precession mode, the field ununiformity brings about some additional complexity in the analysis. However, a precise field map provides necessary inputs to the analysis.

3.2.2 Conceptual design and TOSCA calculation

The basic idea of the magnet system has already been given in the proposal (Fig.5). It consists of 12 identical dipole gaps accommodating the muon stopper in-between. The issues in designing the system were;

- Direction of the field relative to the super-conducting toroidal magnet field. (It was shown to be anti-parallel in the proposal.)
- Question of whether the iron shim plates which played an important role in E246 is necessary or not, and
- Question of whether the two magnetic fields should be separated by clamping the SC (or shim) field by end-plates.

In order to solve these questions, 3D field calculations were performed using the TOSCA/ OPERA code. All the realistic geometry and material conditions were input for the SC toroidal magnet, shim plates, end-plates, and new magnets, and the conditions questioned above were changed and the resultant field distributions were compared. The calculated elements are shown in Fig.5. The criterion was the realization of a smooth and preferably flat field distribution on the stopper volume, especially in the $z-$ (beam) direction. The design that we finally adopted is 1) the parallel field arrangement as opposed to the proposal, 2) no separation of the two fields by the end-plate (This is also a natural consequent of the parallel fields.), and 3) preservation of the shim plates. This third point is important to suppress the effects of not-well known alignment of the SC coils of the toroidal magnet cryostats. The field distribution along z in this case is shown in Fig.6, and the main parameters of the magnets are summarized in Table 6.

3.2.3 Further detailed studies

Along this basic concept, several studies are now going on toward a detailed design of the magnet system. They are;

- Realization of much flatter field distribution on the stopper by applying pole-edge shims. In order to improve the azimuthal field distribution such shims will be very effective. Also a shim at the outer z-edge will be useful.
- Evaluation of the force acting on the SC coils. The SC coils are supported by a kind of Heim columns in the cryostat and not very rigid against an excess magnetic force in z-direction. If the force exceeds a tolerance value, a counter balance has to be mounted on the opposite upstream side.
- Establishment of a mechanical support and the alignment of the system at installation as was described in the proposal. A scheme to ensure access to the inner chambers C3 and C4, and to guarantee alignment reproducibility has to be worked out.

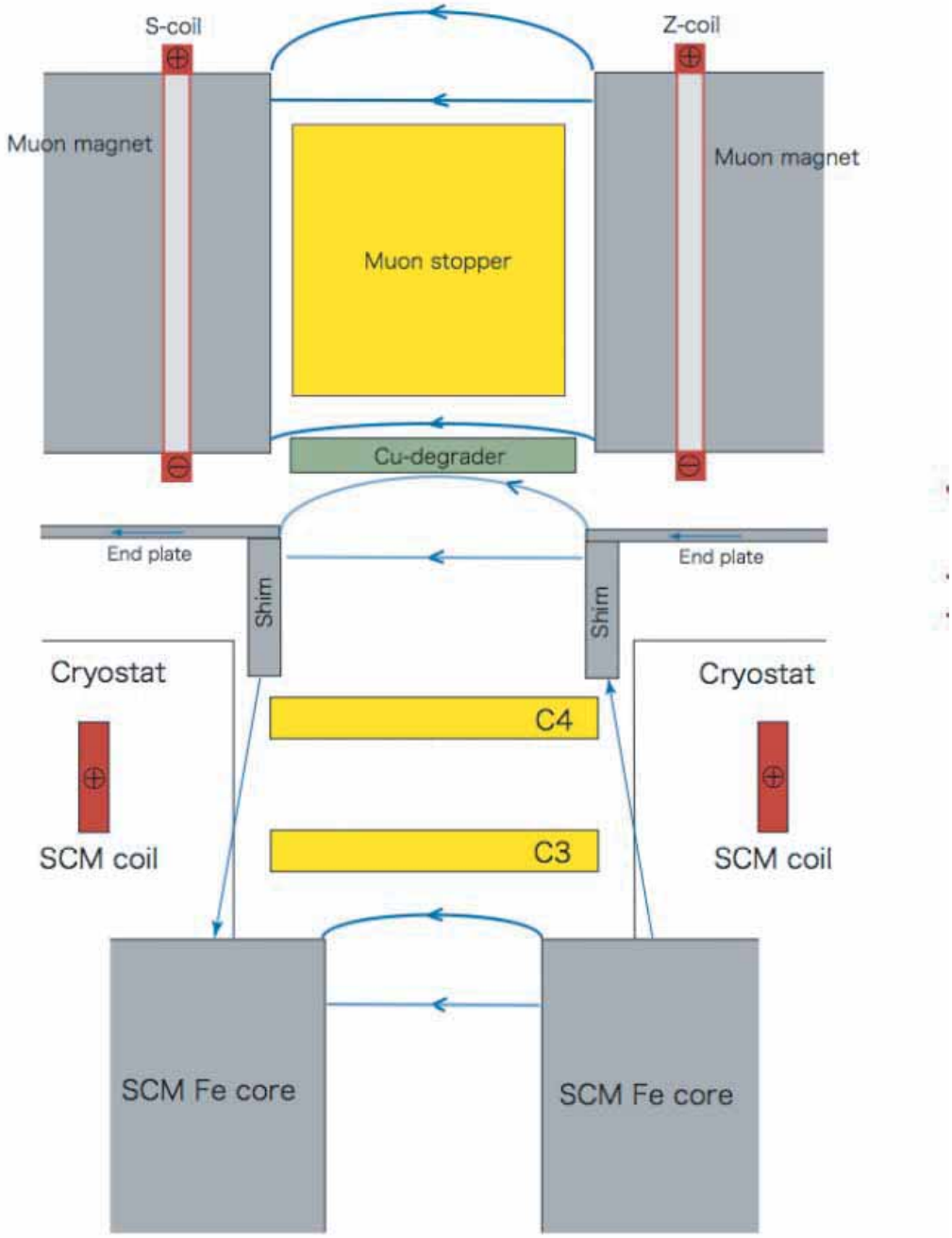

Figure 5: Structure and configuration of the new muon field magnet

Table 6: Main parameters of the muon field magnet

Parameter	Value
B	0.03 T
Gap	30 cm
Pole face	60 $cm^H \times$ 40 cm^W
MMF	7.2 (or 3.6)$\times 10^3$A·turn/coil
Number of coils	12 (or 24)
Coil size	5$\times$ 10 (or 5) cm^2
Power	500 (250) W /coil
Total power	6 kW
Cooling	indirect water cooling
Total weight	5 ton

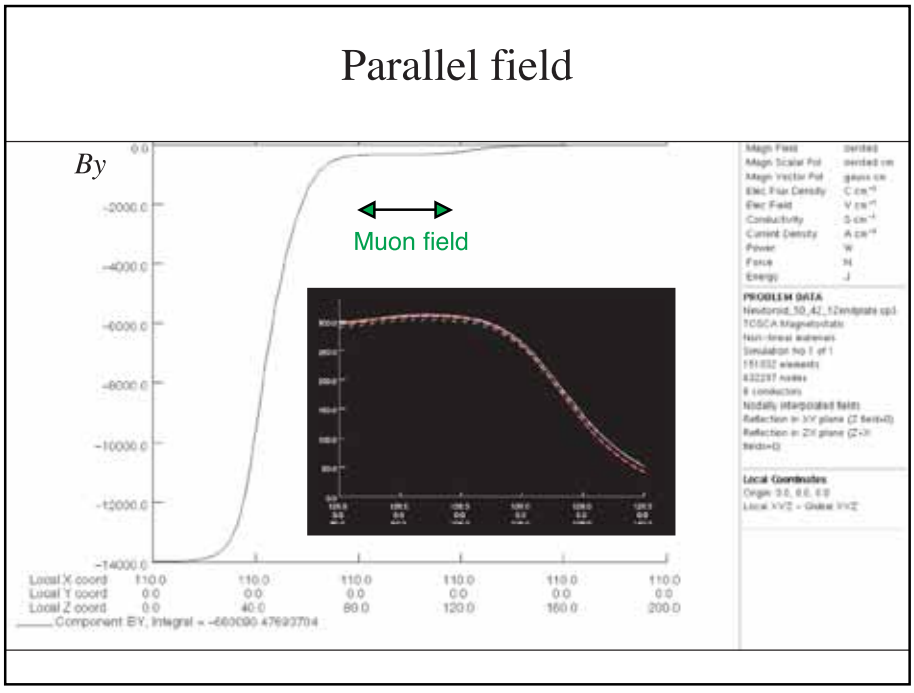

Figure 6: Field distribution on the muon magnet median plane along the z-axis. The black insert is the expansion of the muon field drawn inverted.

Table 7: Main parameters of the CsI(Tl) calorimeter.

Parameter	Value
Number of CsI(Tl) crystals	768
Segmentation	$\Delta\theta = \Delta\phi = 7.5^\circ$
Inner /outer diameter	41 / 90 cm
Detector length	141 cm
Solid angle coverage	$\sim 75\%$
Crystal length	25 cm (13.5 X_0)
Typical size of crystals	$3 \times 3 - 6 \times 6$ cm^2
Wave length at peak	560 nm
Light decay time	~ 900 ns

3.3 CsI(Tl) photon calorimeter

The main task of the CsI(Tl) photon calorimeter is the reconstruction of the momenta of neutral pions from $K^+_{\mu 3}$ mode by detecting the two photons from π^0 decay. The detection of the π^0 determines the $K^+_{\mu 3}$ decay plane and hence the direction of the transverse muon polarization. The reconstruction of the π^0's momentum is also critical for the fwd/bwd cancellation of the systematic errors.

3.3.1 Parameters of CsI(Tl) modules

The photon calorimeter in the E246 setup was a barrel of 768 CsI(Tl) crystals surrounding 75% of total solid angle around the target region. The barrel had 12 muon holes to allow the charged particle enter the spectrometer. The sizes of the muon holes were optimized for the $K^+_{\mu 3}$ acceptance to be maximum. The main parameters of the barrel are summarized in Table 7 and are reported elsewhere [3, 8]. In the previous E246 experiment the light readout with large size PIN photo-diodes (18×18 mm^2 or 28×28 mm^2) was employed. High light collection in a CsI(Tl) module enabled the high light yield (11,000 $p.e.$/MeV) and low noise ($ENL = 70$ keV) for each module. This allowed the measurements with a low photon energy threshold as well as the extraction of the timing information which was applied in the photon trigger and used in the analysis. A moderate time resolution with an average σ =9 ns was obtained. The timing performance was essential for forming a γ-cluster in the presence of accidental backgrounds from the beam pion halo. The energy response function had a significant tail on the low energy side mainly due to shower lateral leakage into the muon holes. Nevertheless, the intrinsic energy resolution of the main part of the spectra is reasonably good. The angular resolution of about 2.3° was essential for the π^0 kinematics determination.

These basic parameters of the E246 photon calorimeter also satisfy the requirements of the E06 (TREK) experiment, which motivated us to use the current CsI(Tl) crystals again after applying one necessary modification. Namely, they must operate at the about 20 times higher beam intensity. Accordingly, an increase in the detector counting rate of a factor of ~ 10 is expected. This corresponds to a maximum rate of 0.1MHz in each crystal or to about 20 MHz of total decay particle rate into the total solid angle of 4π. However,

the E246 readout scheme, consisting of a PIN photo-diode, a charge-sensitive preamplifier, a shaping amplifier and a peak-hold ADC, does not work at the higher counting rate of the J-PARC experiment for the following reasons:

- The width (including the tail) of shaping amplifier output pulse was nearly 15 μs for a shaping time constant of 1μs. Higher rate results in a pileup of events degrading the energy resolution or even spoiling the event identity.
- The maximum acceptable rate of the charge preamplifier was determined by its output dynamic range and signal gain, which is calculated as $r_m = V_m/(QR_f)$ with the maximum voltage V_m, the average input charge Q, and the feedback resistance R_f. Because it was only 34 kHz, a higher rate would cause a loss of events with a significant probability.

Note, that the CsI(Tl) light decay constant of 900 ns itself meets the requirement of higher beam intensity. The slow readout in E246 was conditioned only by the use of a PIN photo-diode that has no an internal amplification and therefore requires a large integration time of 50 μs in the charge sensitive amplifier. Obviously, the present readout scheme must be replaced by a faster system. A reverse-type avalanche photodiode (APD) with large surface area is a natural candidate as was suggested in the proposal. The self-amplification of some 50 makes the amplifier system simpler and faster.

3.3.2 APD readout and its R&D

At present there are a few types of commercially available APDs with multiplication factors of about one hundred with reasonably large sensitive area [12]. Several APD applications to calorimeters in high energy physics experiments are being prepared. One notable example is the adoption of 140 thousand $5 \times 5\text{mm}^2$ Hamamatsu (HPK) S8148 APDs in the CMS experiment [10] for reading out PWO scintillators with the light emission length of 430 nm. The CsI(Tl) peak wave length of 560 nm is much better matched to the APD spectral sensitivity where an average quantum efficiency about 80% is achieved. Although the E06 energy range is two order of magnitude smaller than in CMS, this better matching and higher light emission of CsI(Tl) should lead to a similar performance. The readout of CsI(Tl) by an APD has already been studied in Ref. [11] by using $10 \times 10\text{mm}^2$ HPK S8664 for a small crystals.

In order to check the performance of CsI(Tl)-APD readout for large size crystals we are performing test measurements at INR (Moscow) by using a spare E246 CsI(Tl) module with a typical size. One $5 \times 5\text{mm}^2$ HPK S8148 APD was attached at the rear side of the CsI(Tl) crystal. The APD signal was amplified in two stages. The first stage included a fast amplifier with a gain $\sim$300 initially intended for the TOF system with plastic scintillators. At the second stage the signal was amplified in a commercial CAMAC amplifier with the variable gain and integration time. The long scintillator pulse with small amplitude had significant photoelectron fluctuations and therefore was smoothed by selecting an integration time of 50 ns. The full length of the signal was found to be 1.5μs which is about ten times shorter than in E246 CsI(Tl) calorimeter. This output signal depends on the parameters of the amplifier used and does not completely reproduce the shape of the CsI(Tl) scintillator pulses with the time decay of 900 ns. The APD signal after the amplifiers was recorded in a charge-sensitive ADC. The measured equivalent noise level of about 0.8 MeV indicates the

rather moderate performance of the amplifiers that does not allow the detection of the low energy photons from $\gamma-$sources. The expected light yield of about 930 $p.e./$MeV can be estimated from the simple comparison of the APD active area with that of PIN-photo-diode.

3.3.3 Cosmic ray test of APD readout

The APD readout at higher energies was tested with the cosmic muon trigger selecting the energy deposition in the CsI(Tl) crystal in the range from 15 MeV to 20 MeV. This range of the energies is conditioned by the path length of the muons in the trapezoidal shape crystals. A raw signal (Fig. 7) is significant for this energy range above the noise level. The ADC spectrum of detected energies is shown in Fig. 8. A clear peak with the width of about σ =17 % is visible. Taking into account the spread of the deposited energies the observed resolution is comparable with the 12% obtained in E246 experiment with large PIN-diode readout. Similar energy resolution is expected for larger deposited energies for both cases of APD and PIN-diode. More accurate in-beam tests of the CsI(Tl)-APD readout are required for the careful examination of its performance. Another possible variant is the use of a larger size $10 \times 10\text{mm}^2$ HPK S8664-1010 APD. The four times larger active area of this APDs ensures high light collection at low energies, which was also confirmed in the present test measurement. It is, however, noted that a possible degradation of the energy resolution at low energies should not change the overall performance of the photon calorimeter remarkably, as the escape of the electromagnetic shower into muon holes plays a major role.

In the measurement with cosmic muons the time spectrum was collected as a difference between the trigger signal from the plastic counter and the APD signal from CsI(Tl) module. The obtained distribution is shown in Fig. 9. Here the time resolution of about 3 ns corresponds to 15-20 MeV energy deposition in the crystal. Due to the shorter rise time of APD signal the time resolution is about 4 times better than the previous result obtained with the E246 PIN-diode readout.

3.3.4 Adoption of APD readout

As a summary of this study we can conclude that APD readout of large CsI(Tl) modules is quite feasible and reveals promising results with the following remarks:

- The width of the signal after the amplifier with the optimum response matched to CsI(Tl) light decay constant should be about 1.5 μs and one order shorter than that in the E246 experiment. We might expect an appropriate CsI(Tl) rate capability in the E06 experiment with higher beam intensity. As an additional option we are going to use FADCs with 65 MHz sampling instead of ordinary charge sensitive ADCs. These FADCs are currently being developed at KEK and now will be available for J-PARC experiments. FADCs are very powerful to resolve pileups and we may expect pulse separation for a pileup with a time difference larger than half of the decay time (400 ns).

- The readout with small $5 \times 5\text{mm}^2$ HPK S8148-0505 APD provides reasonable energy resolution for 15-20 MeV energy deposition in CsI(Tl) crystals. It is more cost effective rather than the S8148-1010 APD. The amplifier performance did not allow the careful tests of the resolution for low energy photons from γ-sources at this time.

Table 8: Performance of APD readout of a CsI(Tl) module for cosmic rays (C.R.) compared with the E246 PIN readout: Hamamatsu S8148-05050 is assumed for APD.

Parameter	E06 APD readout	E246 PIN readout
Electron yield	47,000/MeV	11,000/MeV
Noise level	not yet measured	70 keV
Energy resolution	∼12% for C.R.	12% for C.R.
Time rsolution	3 ns for C.R.	12 ns for C.R. (9 ns for all)
Pulse width	~ 1.5 μs	15 μs
Rate performance	~ 500 kHz	34 kHz

- The time resolution of CsI(Tl) modules with APD readout is about 4 times better than that in the E246 experiment. This guarantees us a reliable selection of $\gamma-$clusters and the suppression of the accidental background in the photon calorimeter.

- Another important issue is the development of an amplifier. Due to the internal APD gain of about 50, the circuit design of an such amplifier can be simple. At the moment, a baseline design of the amplifier exists. It consists of an input current amplifier and a signal shaper. A preliminary circuit simulation of this scheme confirms a good capability to resolve 1μs length pulses at a distance of 1.5 μs. Further design and tests of the amplifier are on-going.

- The experimental area will be air-conditioned for constant temperature of $20 \pm 0.5^{\circ}$. Hence, the temperature gradient of the APD gain does not matter.

3.4 Kaon stopping target

3.4.1 Requirements and basic design

The policy for the target upgrade was described in the proposal in detail and will not be repeated here. The main points are:

- Optimization of the size (diameter and length) for the new K0.8 beam for the E06 experiment, which might favor smaller diameter than the E246 target with the 10 cm diameter including the surrounding trigger counters, consisting of 256 fibers of 5×5 mm^2.

- Finer segmentation of fibers to accept higher K^+ beam intensity in a smaller beam spot. Finer fiber size is preferable also from the point of view of decay particle tracking and background rejection, in particular the π^+ decay-in-flight μ^+ from predominant background channel of $K^+_{\pi 2}$.

- According to a MC simulation a kaon decay vertex resolution of $\sigma \sim 0.8$ mm (corresponding to 2.5×2.5 mm^2 fiber cross section is very powerful and necessary to reject this background.

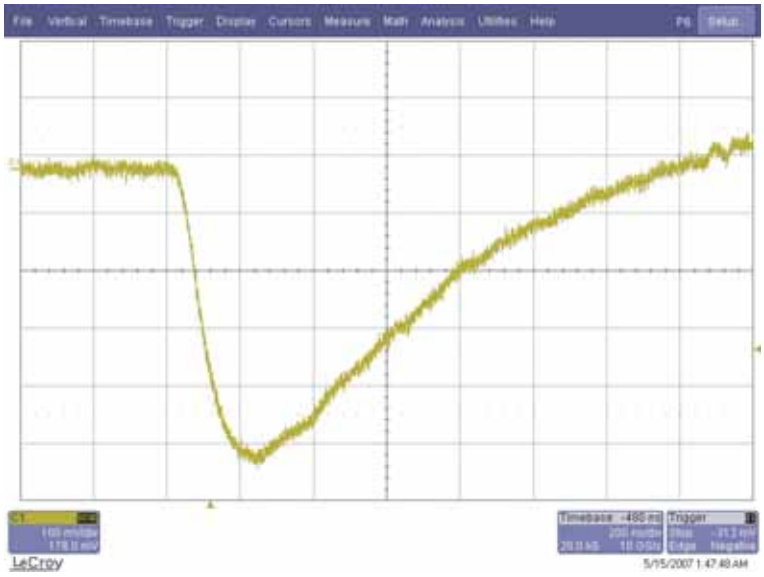

Figure 7: CsI(Tl) raw signal for a typical cosmic ray event read by a $5 \times 5\text{mm}^2$ Hamamatsu S8148-05050 APD. A pulse withs of 1.5μ s was observed with a positive overshoot tail. One horizontal division is 200 ns.

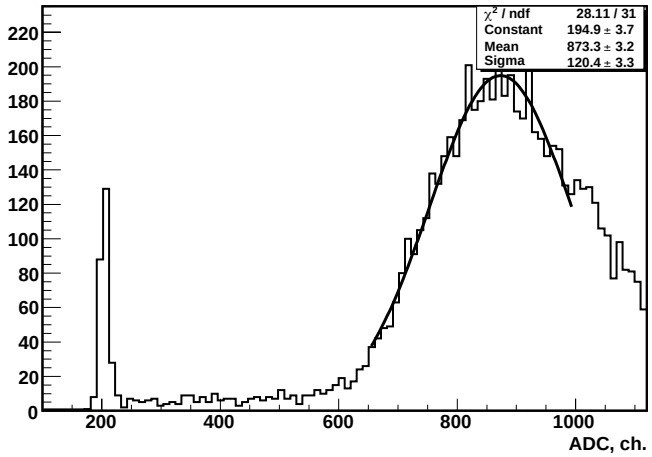

Figure 8: ADC spectrum in CsI(Tl) module corresponds to the 15-20 MeV deposited energies from the cosmic muons. One $5 \times 5\text{mm}^2$ Hamamatsu S8148 APD is used for the CsI(Tl) readout. A clear peak with the width of about σ =17 % is visible.

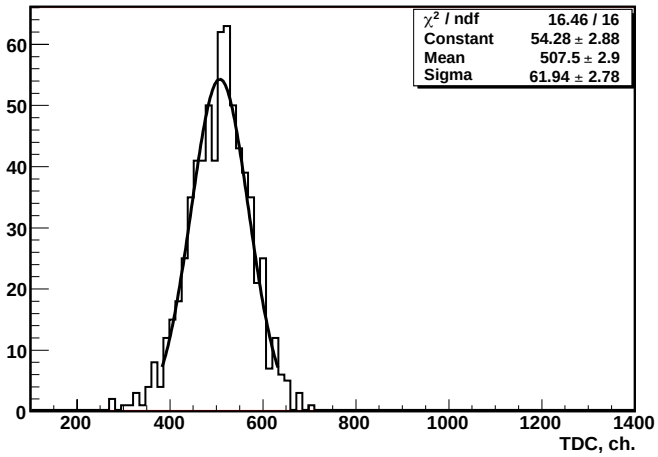

Figure 9: TDC spectrum obtained as a time difference between the signals from the CsI(Tl) module and the cosmic muon trigger counter. One TDC channel corresponds to 50 ps. A time resolution of 3 ns for the 15-20 MeV energy range was observed.

- Realization of a compact and light assembly including readout system, which becomes essential for accurate alignment necessary for this high precision experiment.

The current baseline design is a bundle of 432 scintillating fibers with a size of 2.5 × 2.5 mm^2 and a length of 20 cm surrounded by several trigger counters with the same length. This design calls for gluing each scintillating fiber to a clear fiber of matched cross section and length sufficient to place the readout element in an acceptable radiation environment. This makes a contrast to the E246 target in which each 5×5 scintillating fiber with a length of 185 cm was directly connected to a PMT. As the readout element we consider a Geiger-mode avalanche photo-diode (APD) called SiPTM. MAPD or MPPC, which are quickly developing these days rather than PMTs.

The engineering design and construction will be done in the Detector Development Facility at TRIUMF under the supervision of Robert Henderson. This same group was similarly responsible for the E246 target.

3.4.2 Readout using MAPD/MPPC

The adoption of MAPD/MPPC readout is favored by the considerations about 1) the immunity to magnetic field, which provides more freedom in the detector configuration design, 2) cost effectiveness, and 3) making the total assembly compact and light, which we regard as essential in E06. The temperature dependence problem of the gain is regarded as less problematic since the experimental area is air-conditioned to a constant temperature of 20±0.5° and the temperature of the target MPPC panel is further controlled locally to a few tenth of a degree. The development of commercially available MPPC products is very quick these days in Russia as well as in Japan. The performance of the Hamamatsu (HPK) MPPC with 1×1 mm^2 of 100 or 400 pixels have recently been reported in a workshop [12].

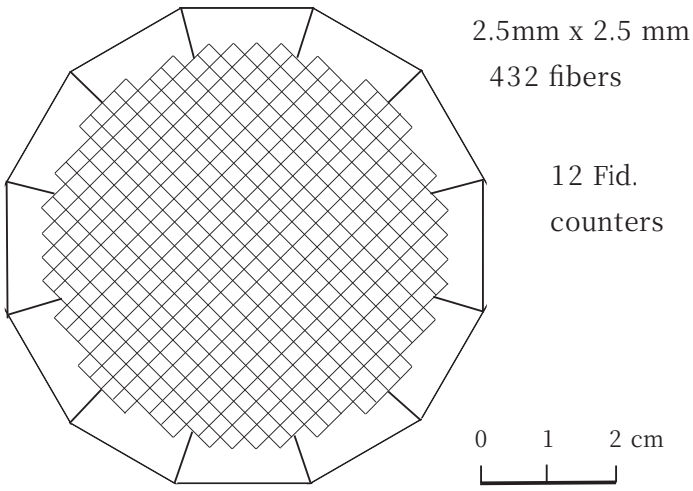

Figure 10: Cross section of the new E06 target

If we adopt the HPK 1×1 mm^2 MPPC with high gain of $\sim 10^6$ which are now commercially available with reasonable price, there are two ways of clear fiber light transmission conceivable. In the proposal we considered using 4 MPPCs for each scintillating fiber by using 1 mm diameter clear fibers. However, the considerations on 1) light yield and 2) cost, led to the current design of one square clear fiber with the same size as the target fiber. The terminal end of this clear fiber will be tapered to 1×1 mm^2 to match an MPPC.

3.4.3 Readout tests

Two tests were performed to check the readout by means of MAPD/MPPC and at the same time to measure the photon yields from the 2.5×2.5 mm^2 thick scintillator stick. One test was performed at INR (Moscow) last year for E06 by using a 20-cm scintillating fiber stick without cladding attached to a 3×3 mm^2 MAPD from Dubna-Micron Co. (Russia) and the average number of photons (*p.e.*) of 35 was observed for ^{90}Sr while the pedestal level was 1.5 *p.e.*. Quite recently in this year another reading has been tested for the HPK 1×1 mm^2 MPPC S10362-11-1010 by using the same stick but with one end tapered to a 1×1 mm^2 cross section. A photon yield of ~ 20 was observed also for ^{90}Sr. The pulse hight spectrum is shown in Fig. 11. These two data are more or less consistent with each other considering the differences in 1) the loss at the taper, 2) the photon detection efficiency (PDE) of MAPD/MPPC, 3) the light reflection method of the stick, and 4) the stick - MAPD/MPPC coupling.

With the help of these data we may estimate the photon yield in the final design to use multi-clad fibers. Each clear fiber will be also multi-clad and with Extra Mural Absorber (EMA) to prevent cross talk. In order to maximize light transmission, the range of taper

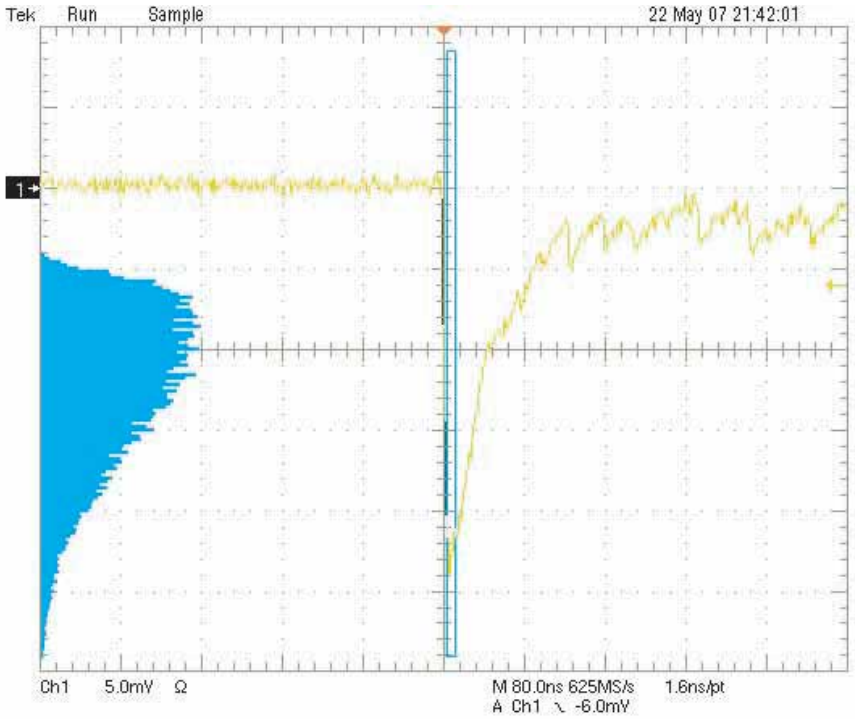

Figure 11: Pulse height spectrum of MPPC S10362-11-1010 reading the 2.5×2.5 mm^2 scintillating stick with 20 cm length irradiated by ^{90}Sr (blue histogram). Vertical axis is the pulse height with the zero base line at the black square. A typical signal form (yellow line) is also shown. From the one-photon and cross talk two-photon peak difference, the average photon yield was evaluated to be ~ 20.

length and shapes should be optimized. Taking into account fiber specification[2], we will assume 80% transmission through the clear fiber including the coupling to MPPC in the present estimation. The transmission-relevant parameters and photon number reduction are summarized in Table 9 showing the feasibility of this scheme.

3.4.4 Radiation hardness of MPPC

One concern about using MPPCs for the target fiber readout is radiation damage. Its radiation hardness is not well studied. Although the radiation environment at K0.8 will be unmeasured constraints, we rely on a GEANT4 simulation to estimate the particle fluxes for the realistic K0.8 beam condition. A momentum degrader made of BeO with 10 cm in diameter to slow down the K^+ beam into the target were assumed. Fig.12 shows the typical flux densities for scattered/reaction-produced particles (only K^+ is shown in the figure) on the plane 70 cm downstream from the setup center for a certain number of incident K^+s.

On the other hand, an experiment was performed at Research Center for Nuclear Physics

[2]Bicron reports the angular spread of a beam in clad fiber at a few degrees so that, given our apertures, the tender would give an exit cone of 5 degrees and after refraction to air, a cone of 8 degrees at MPPC.

Table 9: Light reduction of the scintillating fiber + clear fiber assembly

Parameter	Value	No. of photons
Scintillating fiber	Saint-Gobain (Bicron) BCF-12	
Size	2.5×2.5 mm $\times 20$ cm	
Energy deposit	0.47 MeV for MIP	$\sim 3,780$
Trapping efficiency	6%	227
EMA loss	2%	222
Attenuation and glue joint loss	42%	128
Taper and coupling loss	30%	90
PDE of MPPC	40%	$p.e. = 36$

PDE (photon detection efficiency) includes the quantum efficienct (QE).

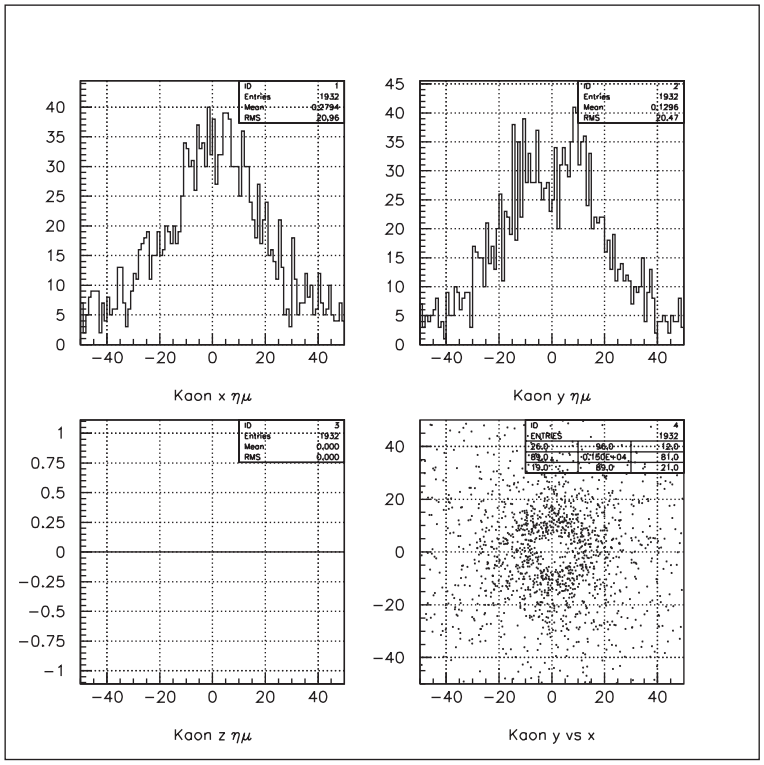

Figure 12: Particle flux distribution around the target calculated with a GEANT4 simulation calculation. For this figure only the kaon flux at $z = 70$ cm is plotted. The distributions of other particles, π^+, μ^+, e^+ and n are similar. A BeO degrader of 10 cm in diameter with a length of 49 cm was assumed in front of the target.

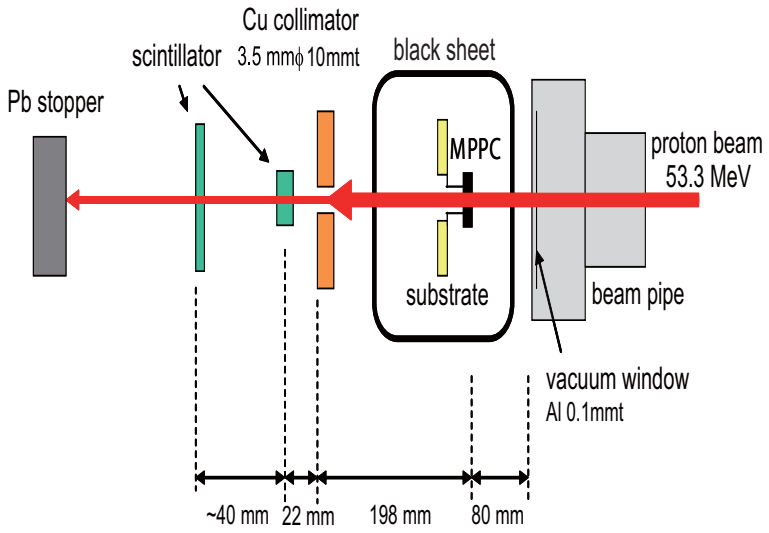

Figure 13: Experimental setup of the MPPC irradiation test at RCNP. The collimated proton beam with 53.3 MeV struck the MPPC. The integrated irradiation dose was counted by the two plastic scintillators.

(RCNP) to investigate actually the radiation damage due to hadrons. Four E06 members participated in this experiment. Two samples of MPPCs, HPK S10362-11-050C, were irradiated by a proton beam with the energy of 53.3 MeV as shown in Fig. 13. Variations of the leakage current of the MPPCs were measured using beams of (a) 2.3×10^5 protons/mm^2/s and (b) 3.0×10^4 protons/mm^2/s fluxes. Preliminary results indicate that the leakage current increases with increasing the total irradiation dose (nearly proportional), being independent of the instantaneous beam flux. According to the above mentioned simulation calculation, this tested integrated dose would correspond to roughly several months of 9 μA operation assuming 20 cm off axis for the MPPC position. The noise rate due to the dark current is now being checked to determine whether or not it is in a tolerable range. If it would be serious, we have to put some shielding in front of the MPPC panel to suppress the beam related radiations to a harmless level.

3.4.5 Consideration on pixel size

There are two conditions to determine the pixel size of the MPPC. One is the dynamic range for energy measurement, since we are going to measure not only minimum-ionizing traversing decay particles from stopped kaon but also a large energy deposit of stopping kaons. A dynamic range of 10^2 is required. For this purpose MPPC with a larger pixel number is preferable. We will use the MPPC with 400 pixels from this viewpoint at the cost of gain. We are going to install two sets of amplifiers and ADCs[3] for two very different signals.

The second point is the rate performance. A fairly long recovery time of each pixel of

[3]In practice we will adopt a QTC+TDC scheme for ADC.

about 100 μ s was reported [13] for some types of the HPK MPPC with 100 pixels. Each fiber has to accept 10^5 particles per second. The recovery time of each single cell is then required to be 1.0 to 0.1 μs range. It is very desirable to select an MPPC with a large number of pixels such as 400 or 1600, which have the recovery time of this range. If the number of the pixels is large enough the probability for a certain pixel to be hit subsequently becomes smaller and the effective dead time of the MPPC becomes accordingly small.

3.5 Charged particle tracking system

3.5.1 Requirement for the tracking system

The necessity for a tracking system upgrade was discussed in detail in the proposal. In the E06 experiment, the systematic errors on P_T need to be suppressed to the 10^{-4} level. In order to achieve such an error level, a significant upgrade of the E246 tracking system is required. The capability to perform high-resolution tracking (momentum, angle, and vertex) of charged particles from K^+ decay in a momentum range of 100-250 MeV/c by means of the SC Toroid is a powerful aspect of the E06 experiment. Briefly:

- High momentum resolution is necessary to distinguish the two-body decay channels $K_{\pi 2}$ and $K_{\mu 2}$ from three-body decays to suppress background in the $K_{\mu 3}$ sample.
- A well defined angle of the charged particle along with the reconstructed π^0 angle are important to obtain a good $K_{\mu 3}$ kinematical resolution. Good angle resolution is also required to select back-to-back $K_{\pi 2}$ events for calibration.
- Excellent vertex and angular resolution is required to identify events from pion decay in flight ($K_{\pi 2}$-dif). Since these events present a background that has a transverse polarization component, they should be sufficiently suppressed.

3.5.2 New tracking system

The new system is characterized by following points:

- Thinner target, higher segmentation (6 cm instead of 9.3 cm wide with a segmentation of 2.5×2.5 mm^2 fibers instead of 5×5 mm^2,
- Helium bags in the magnet between C2 and C3 and before C2 to reduce multiple scattering along the path.
- Increase of the distance between C3 and C4 to 22 cm to provide more leverage for efficient momentum tracking.
- Addition of a cylindrical chamber "C0" based on triple-GEM technology surrounding the target at a small radius of about 7 cm
- Addition of a planar triple-GEM chamber "C1" outside each CsI(Tl) gap at a radius of ∼50 cm to reserve redundancy in the analysis.

Figure 14 shows a comparison of the tracking system in E246 and the E06 (TREK) experiment. The main feature is the addition of C0. For sufficient identification and suppression of $K_{\pi 2}$ events it is required to build a cylindrical tracking chamber ("C0") with a radius of about 7 cm surrounding the target and with a spatial resolution of <0.1 mm. Four-point tracking including C0 should significantly enhance the achievable resolution for track momentum and origin at the target. C0 is exposed to not only decay particles from

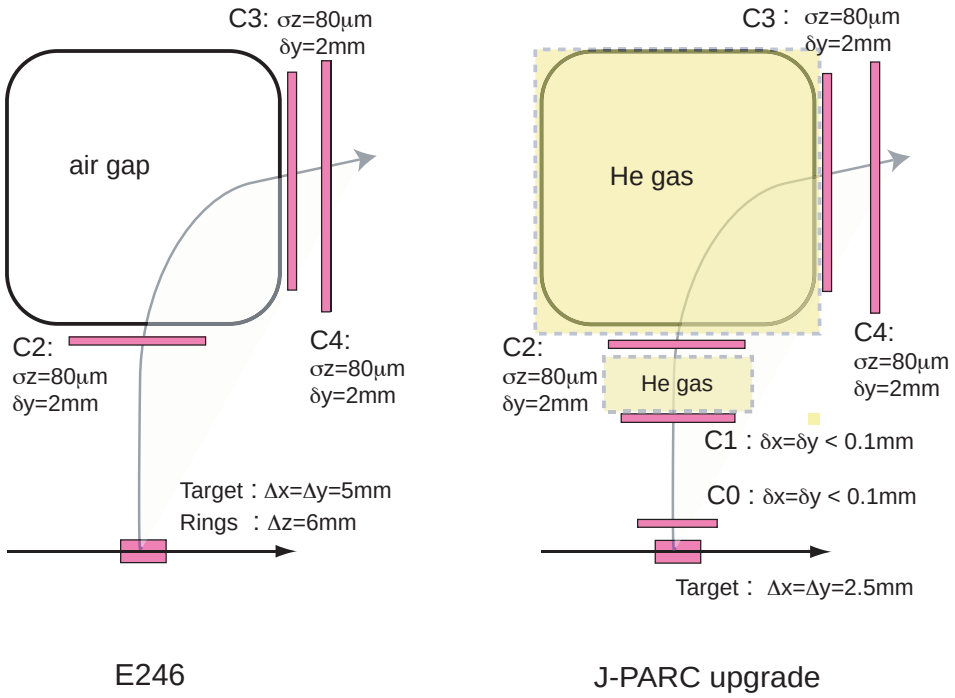

Figure 14: Schematics of the tracking system in the E246 setup (left) and the proposed setup for E06 (TREK) (right).

Table 10: Main parameters of the planar MWPCs Image

Parameter	Value
Anode wires	20 μm diameter Au-coated W
Anode pitch	2 mm
Half gap	6 mm
Cathode strips	9-mm width with 1-mm spacing
Effective area	
C2 (rate/wire)	16×56 cm^2 ($\sim$380/s)
C3 (rate/wire)	20×64 cm^2 ($\sim$100/s)
C4 (rate/wire)	20×72 cm^2 ($\sim$100/s)
Gas mixture	Ar: Ethane 50:50
Readout	x, y cathode strips

the target but also to a beam halo. It has to withstand the expected beam related intensity at J-PARC in the 10^6 Hz region. A new planar tracking element (again named "C1") increases redundancy with <0.1 mm resolution to cover each of the 12 gaps at the outer surface of the CsI(Tl) calorimeter. For C2, C3 and C4, the existing E246 chambers will be reused, since they have still margin in rate performances. The main parameters of these MWPCs are summarized in Table 10. The maximum rate/wire was estimated for the K0.8 beam intensity at the Phase 1 accelerator operation.

The new tracking elements C0 and C1 will be based on GEM technology (Gas Electron Multiplier) which has recently become available. GEM detectors for charged-particle tracking present a new generation of position-sensitive counters which are reasonably cheap, radiation-hard and well suited to be operated in high-rate environments. A high-rate capability in excess of 100 kHz/mm^2 has already been demonstrated within five year operation with no evidence for aging. They are highly efficient even for minimum ionizing particles and can easily be built with spatial resolution of better than 0.1 mm with a small material budget. Both planar and cylindrical geometries with curved GEM foils are possible.

3.5.3 C0 and C1 GEM chambers

It is quite feasible to construct a cylindrical triple-GEM chamber without an azimuthal dead angle; the technique is explained in Appendix B. The main information provided by the cylindrical C0 element surrounding the target will be the vertex position along the target z-axis and a precise value of the azimuthal angle of the outgoing charged track, which will allow us to precisely determine the closest transverse distance, K_{diff} (see below for definition), of the track from the beam axis. The radius of C0 is determined from the following considerations:

- In order to identify $K_{\pi 2}$-dif events as much as possible, a smaller radius is preferable. It is impossible to reject the μ^+ from π^+ decay between the target and C0 in the χ^2 analysis of the tracking chambers. The number of such events within a radius of 10 cm amounts to about 1% of the total $K_{\pi 2}$ yield.

Table 11: Main parameters of the C0 chamber.

Parameter	Value
Outer radius (readout layer)	7.0 cm
Inner radius (drift layer)	5.5 cm
Active length	30 cm
Thickness as standard TGEM	0.70 $\%X_0$
Thickness as light TGEM	0.20 $\%X_0$
2D readout azimuthal + longitudinal, pitch	635 μm
Number of channels	$\sim$ 1200
Position resolution	50-100 μm

- A minimum bending radius for the GEM and readout foils for safe operation and easy handling are also set a lower limit on the C0 radius.
- The whole C0 assembly is inserted to the inner diameter of the CsI(Tl) barrel which is 25.0 cm.
- According to the current design the target has an outer dimension of 75 mm including the trigger shell.
- The possible size of any strong beam halo is to to be avoided.

The current baseline design takes 7.0 cm for the outer radius of readout layer and 5.5 cm for the inner diameter of drift layer. Table 11 summarizes the properties of the proposed C0 chamber. A detailed description can be found in Appendix B. An important aspect is the material budget requirement of the C0 chamber. Here, the cylinder surface including all GEM and readout foils and carrying materials have to be as thin as possible. The material budget of the current design which was mostly adopted for the MIT prototype amounts to 0.70% X_0; however it also offers a lot of potential to significantly reduce the material down to 0.20% by using much thinner copper layer (1 μm instead of 5 μm) and by adopting the double-GEM design. This requirement also implies that all readout electronics and support structures have to be restricted to the end caps. Two dimensional readout will be done.

C1 will be at the muon holes of the CsI(Tl) calorimeter. Individual light-weight double or triple-GEM planar detectors are considered. The area to be covered for each hole is $\sim$15$\times$45 cm^2. The radial distance of the C1 element will be at $\sim$50 cm from the beam axis. The geometry of the CsI(Tl) muon holes allows for a two-dimensional readout on the sides of the active rectangular regions in the shadow region of the CsI crystals. The existing MIT prototype (presented in the section on R&D below) is already quite close to the design requirements. An important aspect is the light-weight construction with a minimized material budget in the active area. In the standard design it is 0.70 $\%X_0$ as C0 but in an advanved design it can be as thin as 0.11$\%X_0$. Table 12 summarizes the properties of the proposed C1 element.

MIT has recently established a GEM laboratory to perform R&D on GEM detectors for the planned tracking upgrade of the STAR detector at RHIC [14]. We propose to utilize and extend the present R&D activities at MIT with the goal to develop and build the C0 and

Table 12: Main parameters of the C1 element.

Parameter	Value
Area	15×45 cm^2
Thickness as standard TGEM	0.70 $\%X_0$
Thickness as light DGEM	0.11 $\%X_0$
2D strip readout, pitch	635 μm
Number of channels	$\sim$ 1000
Position resolution	50-100 μm
Number of elements	12

Table 13: Comparison of the tracking performances for the E246 and E06

	ΔP_{gap}	ΔP_{loss}	ΔP_{cor}	ΔK_{diff}	A_{diff}	$K_{\pi 2}$-dif BG
E246	1.0 MeV/c	2.5 MeV/c	2.5 MeV/c	20 mm	$\sim 2.0^\circ$	2.4%
E06 (TREK)	0.5 MeV/c	0.85 MeV/c	1.0 MeV/c	0.6 mm	0.3°	0.2%

C1 tracking elements for TREK. Such a strategy of combining the R&D efforts to enable the application of the same technology in two different experiments, namely at RHIC and at J-PARC, has the great benefit of synergistic effects where expertise and effectiveness can be enhanced.

3.5.4 Expected performance and background rejection

The tracking performance was checked by a Monte Carlo simulation using $K_{\mu 3}$ events. Four elements, C0, C2, C3, and C4 were used with their expected performance. The radius of 5 cm was assumed here for the C0 readout layer. C1 was not included, which ensures that the obtained result is a conservative estimate of the system performance. Fig. 15 shows distributions of (a) χ^2, (b) difference of true and measured momentum, (c) distance between the trajectory and the K^+ decay position (K_{diff}), and (d) difference of true and measured μ^+ angle at the decay position (A_{diff}). The P_{gap}, K_{diff}, and A_{diff} resolutions are obtained to be 0.5 MeV/c, 0.6 mm, and 0.3°, respectively. Then, the original momentum (momentum at birth), P_{cor}, is calculated from P_{gap} by correcting for the momentum loss P_{loss} in the target as,

$$P_{cor} = P_{gap} + P_{loss}. \tag{4}$$

The path length in the target obtained from the charged particle trajectory and K^+ decay positron is used for the P_{loss} correction. The P_{cor} resolution is estimated to be 1.0 MeV/c which is dominated by the P_{loss} fluctuation of $\Delta P_{loss} = 0.85$ MeV/c. In order to check the improvement of the present tracking system, we compare the tracking performance of the present E06 with the previous E246, as summarized in Table 13. Needless to say that the significant improvements of ΔP_{loss} and ΔK_{diff} are due to the C0 addition.

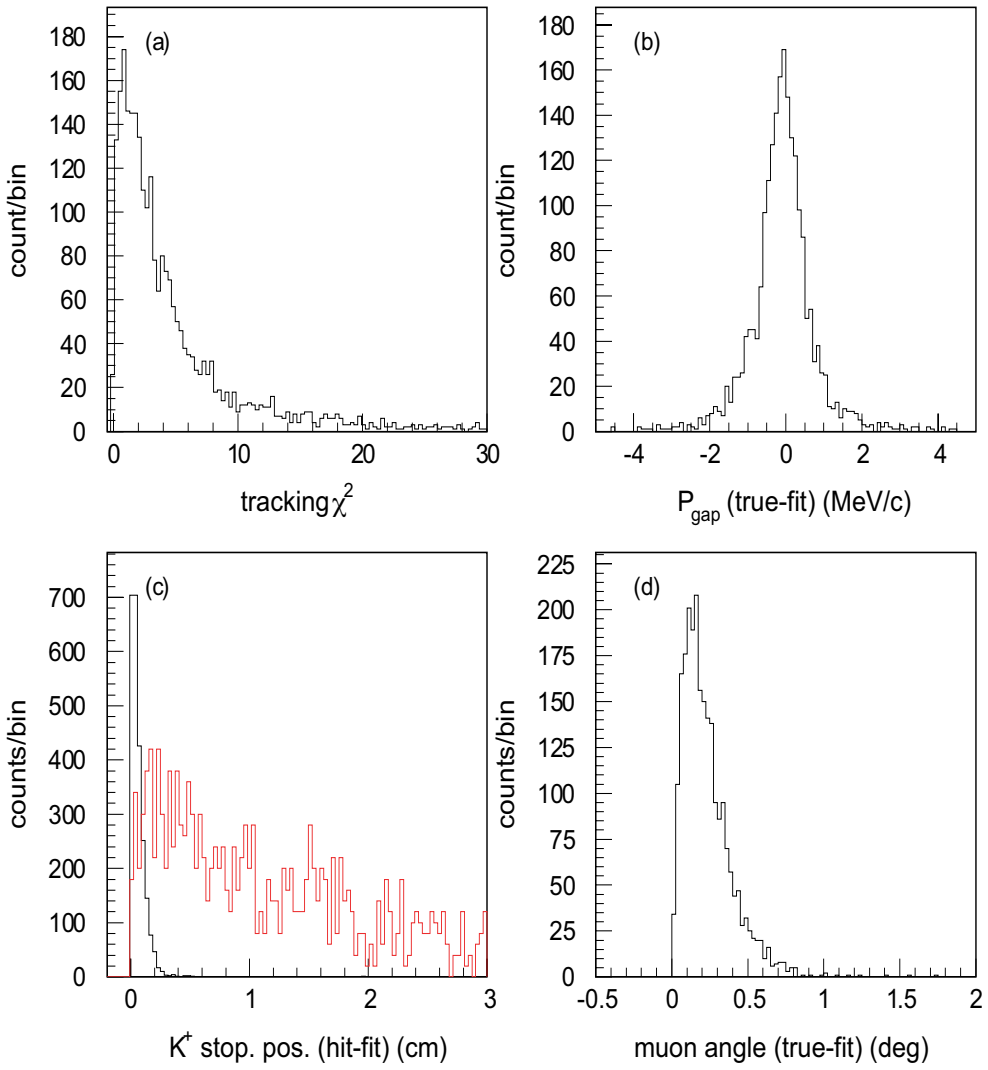

Figure 15: Tracking performance: (a) χ^2, (b) difference between true and measured momentum, (c) distance between the trajectory and the K^+ decay position (K_{diff}), and (d) difference between true and measured μ^+ angle. In-flight $K_{\pi 2}$ events are shown in (c) as red histogram.

An important aspect of the new tracking system is the ability to cleanly suppress background events of $K_{\pi 2}$-dif. Basically π^+-dif beyond C0 can be easily identified by χ^2 of tracking and we can reliably reject those events. However, for π^+-dif events between the target and C0 the χ^2 cut does not work anymore, and only the reliable information for the rejection is the transverse difference of a fit trajectory and a decay vertex in the target, K_{diff}. Fig. 15(c) shows the K_{diff} distribution for $K_{\mu 3}$ (black) and $K_{\pi 2}$-dif (red). The $K_{\mu 3}$ events are selected by requiring $K_{diff} < 1.8$ mm and the $K_{\pi 2}$ fraction in the $K_{\mu 3}$ sample is estimated to be 0.2% which is sufficiently small to achieve a systematic error less than 10^{-4}, because the further cancellation by gap L/R symmetry should be nearly a factor of 10^2. Here it should be noted that the introduction of C0 plays a very important role for the $K_{\pi 2}$ suppression. Even if the C0 radius becomes 7 cm, it is anticipated that the rejection power will not decrease substantially.

3.5.5 GEM chamber test

During the first half of May 2007, an array of three MIT-prototype triple-GEM detectors built with GEM foils by Tech-Etch [14] has been tested extensively along with the new readout system under real experiment conditions at the Meson Test Beam Facility at Fermilab. This prototype can be applied to C1. A comprehensive test program covered voltage, impact position and angle scans to study the gain, efficiency, position resolution and rate capability. It was also the first test of the readout system based on APV25 front-end chip technology [15] in a real experiment environment.

Preliminary results indicate a stable operation of the detectors. A fast offline analysis with primitive cluster finding on data without pedestal subtraction and noise correction was carried out to evaluate the detector performance. Fig. 16 (b) shows the correlation of cluster amplitudes between readout coordinates of one detector together with the distributions of amplitudes. Good charge sharing between planes is apparent, as well as the expected Landau distribution of the cluster charge. Fig. 16 (c) shows the track position residuals in the middle detector of the setup, given by the difference of the position measured in the middle detector and the expected position determined by the two outer detectors. This first analysis, without final alignment and data corrections indicates a spatial resolution of better than 90 μm. Significant improvements are expected with more advanced analysis techniques.

At the end of the test run, the beam intensity was maximized with focused beam yielding $\simeq 2 \cdot 10^5$ protons within 4 s spills, in order to study the rate capability. The time structure of the spill was such that the peak instantaneous intensity is $5 \times 10^5 \sim 5 \times 10^6$ kHz. The size of the beam was 100 mm^2 or less. Therefore the chambers were proved to work at least at 5 kHz/mm^2. Although this is much smaller than the reported performance of COMPASS GEM chamber (100 kHz/mm^2), it is high enough for the expected decay particle rate of the order of 100 Hz/mm^2 in E06 (TREK). The effects of traversing beam halo particles parallel to the GEM plane is now being investigated from the data interpretation.

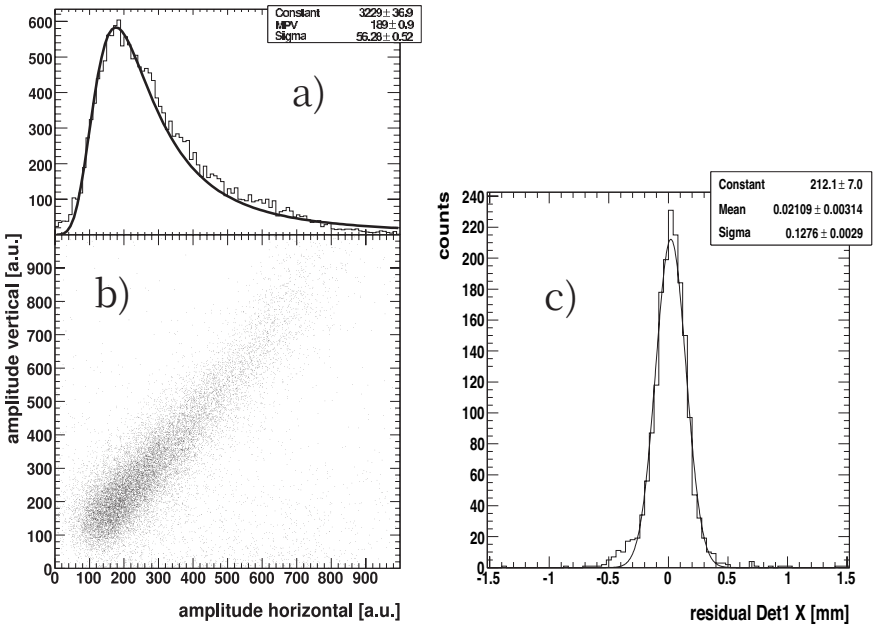

Figure 16: (b) Correlation of hit amplitudes between the horizontal and vertical readout coordinates. The results are based on a very preliminary analysis of not pedestal subtracted data with primitive cluster finding. Good charge sharing between the readout planes is apparent. (a) is the projection of (b). (c) Residuals of tracks in the middle detector of the test beam setup. The results are also based on a very preliminary analysis. The observed width of the distribution corresponds to a spatial resolution of 90 μm.

3.6 Alignment

3.6.1 General method

Along with the "decay plane rotation"[2] due to decay kinematics distortion, the major sources of systematic errors in E246 which are also relevant in E06 (TREK) the misalignments of the detector elements which induced a small admixture of large in-plane polarization components into the transverse P_T component. Fortunately, we could estimate them by actual position measurements of each detector element with a typical precision of 10^{-3}. Since the associated P_T errors were less than 10^{-3}, namely smaller than the statistical error of E246, the effects of misalignments were not used for the correction of P_T but treated simply as items of systematic errors contributing to the total systematic error through a quadratic sum. E06 is aiming at 10^{-4} of the sensitivity, hence, this method does not work anymore. Therefore, we have to perform alignments using the main run data as well as employing special calibration runs.

As was discussed in the proposal in some details, the alignments of the tracking system

and the CsI(Tl) calorimeter system relative to the reference system of the spectrometer will be performed using a set of calibration collimators for the former and $K_{\pi 2}$ events for the latter. Although careful designs are required for both, we regard their calibration procedure rather straightforward; the performance of the calibration can be easily checked with simulations. On the contrary, the effect of polarimeter misalignments, which are direct systematics affecting the positron asymmetry, A_T, are complicated with entanglement of several factors including the muon field. Moreover, one of the misalignments, the rotation of the muon field around the z-axis, is a systematic which cannot be canceled out in the normal π^0 forward/backward subtraction scheme. In this report we present the alignment method of the polarimeter, which is most important and most difficult.

3.6.2 Polarimeter alignments and positron asymmetry

The basic idea of the polarimeter alignment was also given in the proposal. Here, we would like to proceed with that argument further and present a method to extract P_T regardless of the presence of polarimeter misalignments and to determine the degree of misalignments at the same time. A Monte Carlo calculation (The details are described in Appendix A) verifies the validity of this method.

As was discussed in the proposal, the misalignments of the polarimeter are characterized by four parameters of 1) global rotation of the active stopper around the r-axis: ϵ_r, 2) global rotation around the z-axis: ϵ_z, 3) global rotation of the muon field distribution around the r-axis: δ_r and 4) global rotation around the r-axis: δ_z (See Fig. 32 of the proposal). They are only responsible for spurious A_T; parallel displacements should not play a role as long as the active stopper covers the whole muon stopping region because of parallel-shift symmetric structure. The rotation about the y-axis should not have an effect since it brings about only a rotation in the stopper planes.

When these four misalignments exist a precession pattern with a small amplitude appears in the e^+ left/right asymmetry. For the typical two cases of in-plane polarization of longitudinal polarization P_l and radial polarization P_r. The asymmetries can be written as

$$A(P_l) = \alpha_0\{(\epsilon_r - \delta_r)\cos\omega t + (\epsilon_z - \delta_z)\sin\omega t + \delta_r\} \quad (5)$$

$$A(P_r) = \alpha_0\{(\epsilon_r - \delta_r)\sin\omega t - (\epsilon_z - \delta_z)\cos\omega t - \delta_z\} \quad (6)$$

Here, ω is the muon spin precession angular velocity, and α_0 is the asymmetry coefficient for these rotations[4]. More generally, the asymmetry A can be expressed for arbitrary initial muon spin phases θ_0 in the median plane (as shown in Fig. 17) as:

$$A(\omega t, \theta_0) = \alpha_0\{(\epsilon_r - \delta_r)\cos(\omega t - \theta_0) + (\epsilon_z - \delta_z)\sin(\omega t - \theta_0) + \delta_r\cos\theta_0 - \delta_z\sin\theta_0\} + \gamma \quad (7)$$

Here we add an additional offset term γ due to a possible asymmetric muon stopping distribution in the stopper or some unknown polarimeter defects such as chamber inefficiency. Rotation of the magnetic field generates the constant $\delta_r\cos\theta_0 - \delta_z\sin\theta_0$ term which mimics the actual T-violation effect. In the proposal we showed a possibility to use $K_{\mu 2}$ and $K_{\pi 2}$-dif to produce P_l and P_r, respectively. Here, we present another method to use

[4]These equations are the same as Eq.(30) of the proposal in which α_0 was omitted just for simplicity.

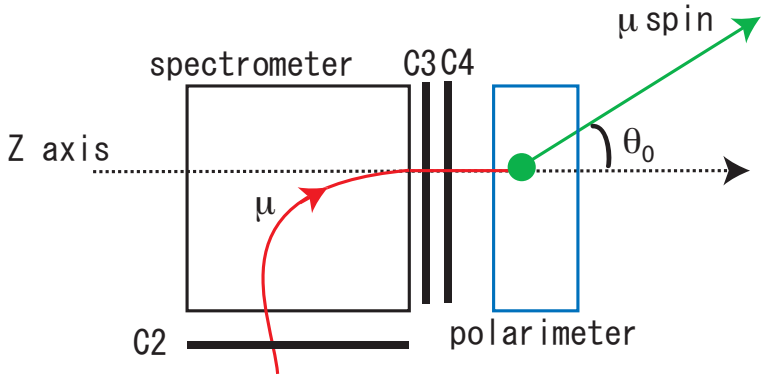

Figure 17: Definition of θ_0 angle. The original muon spin direction was obtained from the kinematics of $K_{\mu 3}$ decay products with a form of [1]. The θ_0 value of each $K_{\mu 3}$ decay at muon stopped position in the polarimeter is determined by taking into account the muon spin rotation by the spectrometer field.

$K_{\mu 3}$ events of the main data. We now regard it as more promising, since it does not require special runs with modified experimental conditions, and it is also not limited by statistical accuracy as in the case of $K_{\pi 2}$-dif.

3.6.3 Alignment analysis in terms of muon spin direction

When we apply this method of analyzing the θ_0 dependence, the $K_{\mu 3}$ events can be used fully. For each $K_{\mu 3}$ event, θ_0 can be calculated from the decay kinematics as is explained in Appendix A.5. In order to simplify the analysis, the time integrated asymmetry was introduced as follows.

$$\begin{aligned} A(\theta_0) &= \int [\alpha_0\{(\epsilon_r - \delta_r)\cos(\omega t - \theta_0) + (\epsilon_z - \delta_z)\sin(\omega t - \theta_0)]dt \\ &\quad +\delta_r\cos\theta_0 - \delta_z\sin\theta_0\} + \gamma, \end{aligned} \tag{8}$$

The oscillation terms are averaged out by the time integration and becomes less harmful compared with the non-oscillating terms. The contribution due to imperfect cancellation of the oscillation term (η) can be described as a function of θ_0 and the time integrated asymmetry is thus rewritten as,

$$A(\theta_0) = \alpha_0\{\delta_r\cos\theta_0 - \delta_z\sin\theta_0 + \eta(\theta_0)\} + \gamma, \qquad \eta << \delta \tag{9}$$

which is a rather simple form compared with Eq.(8). The ϵ terms can be removed by the time integration. Here it should be noted that the spurious asymmetry from the misalignments depends only on θ_0.

In order to extract the misalignment parameters δ_r and δ_z in the presence of a real P_T, we now calculate two asymmetries A_{sum} and A_{sub} as functions of θ_0 such as the sum and difference of A_{fwd} and A_{bwd} with the asymmetries at the forward and backward pions,

respectively. This leads to

$$A_{sum}(\theta_0) = (A_{fwd} + A_{bwd})/2 = \alpha_0\{\delta_r \cos\theta_0 - \delta_z \sin\theta_0 + \eta(\theta_0)\} + \gamma \quad (10)$$

$$A_{sub}(\theta_0) = (A_{fwd} - A_{bwd})/2 = F(P_T, \theta). \quad (11)$$

Here, $F(P_T, \theta_0)$ is the A_T asymmetry function only from P_T origin and it does not involve any misalignment effect. Thus, we have no effects of P_T in A_{sum} and no effects of misalignments in A_{sub}, enabling us the determination of $F(P_T, \theta_0)$ unaffected by the misalignments. From $F(P_T, \theta_0)$ (which is nearly an even function of θ_0), P_T can be deduced, Further, δ_z and δ_r can be also individually determined by fitting A_{sum} with $\cos\theta_0$ and $\sin\theta_0$. The behaviours are shown in Fig. 18 (a) for A_{sub} and Fig. 18 (b) for A_{sum} for Monte Carlo simulation data which we describe next,

3.6.4 Monte Carlo simulation

How this analysis scheme works was checked with a MC simulation, whose details are described in Appendix A. Briefly it is explained as follows. Assuming the existence of both Imξ and δ (with exaggerated values) at the same time, the above A_{sum} and A_{sub} were calculated. Fig. 18 (a),(b) shows the A_{sub} and A_{sum} distributions, respectively, corrected for the analyzing power of the polarimeter as, black circle: Im(ξ)=0.05, $\delta = 0$, blue circle: Im(ξ)=0.05, $\delta_z = 5^\circ$, blue triangle: Im(ξ)=0.05, $\delta_r = 5^\circ$, and red circle: Im(ξ)=0.05, $\delta_z = 5^\circ$, $\delta_r = 5^\circ$. Although they were obtained with various combinations of Imξ and δ, in any cases, the P_T and δ effects were successfully determined by the A_{sub} and A_{sum} analyses. The A_{sub}^{av} and A_{sum}^{av} values with the simultaneous existence of Imξ and δ were compared with those with single Imξ or δ cases, as shown in Fig. 18 (c),(d). They are consistent within errors, indicating the validity of the $A_{sub}(A_{sum})$ scheme to cancel out the misalignments (T-violation) and extract T-violation (misalignment) effect.

For the planned run time we may expect by scaling this result statistically the alignment accuracy of $\Delta\delta_r \sim \Delta\delta_z \sim 3 \times 10^{-4}$ from the analysis of A_{sum} shape, as well as the P_T accuracy of 1.2×10^{-4} from A_{sub}.

3.6.5 Systematic errors

In this simulation study, we used a much exaggerated assumption of $\delta_z = 5^\circ$ and $\delta_r = 5^\circ$. However, the averaged A_{sub}^{av} value with this assumption was $A_{sub}^{av} = 2\times10^{-4}$. The actual field rotation is expected to be at the level of $\sim$1mrad, which is much smaller than the present assumption. Therefore, taking into account the cancellation power of the A_{sub} analysis for the spurious e^+ left/right asymmetry, the systematic error due to the field misalignment is estimated to be less than $\Delta P_T < 10^{-4}$.

Also, the misalignment measurement by the A_{sum} analysis can assure the reliability of the δ determination by checking the consistency with the results from $K_{\mu 2}$ and $K_{\pi 2}$-dif data (See Appendix A.8). Therefore, from both (1) cancellation of the misalignment effects by A_{sub} and (2) understanding of the misalignments by A_{sum}, we can reliably control the systematic error from the field misalignment to a negligible level.

There is a new potential source of error which was not present in E246, namely the error coming from the active polarimeter analysis. Effects from θ_0, E_{e^+} and θ_{e^+} ambiguities were investigated by smearing their quantities in the simulation and concluded to be small. Other

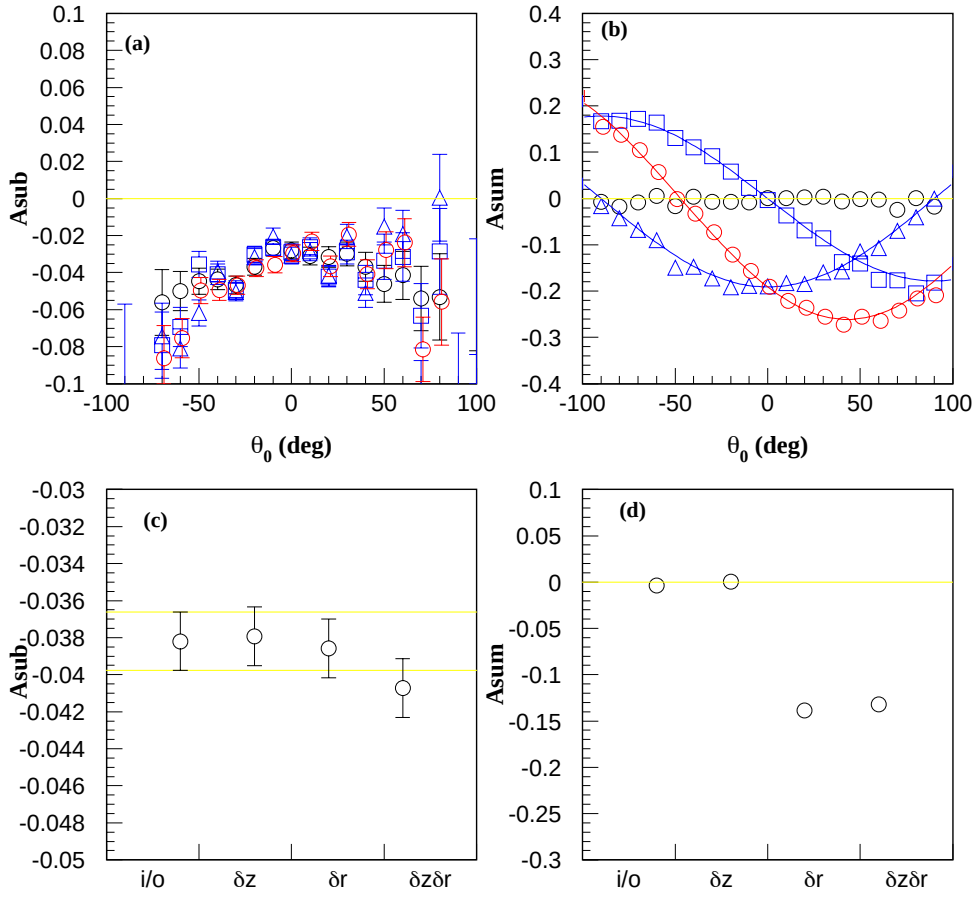

Figure 18: (a),(b) Muon polarization distribution derived from A_{sub} and A_{sum} with various conditions and (c),(d) their error weighted averages, black (ID=1): Im(ξ)=0.05, $\delta = 0$, blue circle (ID=2): Im(ξ)=0.05, $\delta_z = 5°$, blue triangle (ID=3): Im(ξ)=0.05, $\delta_r = 5°$, red (ID=4): Im(ξ)=0.05, $\delta_z = 5°$, $\delta_r = 5°$. The polarization was converted from the e^+ asymmetry corrected for the analyzing power α_0.

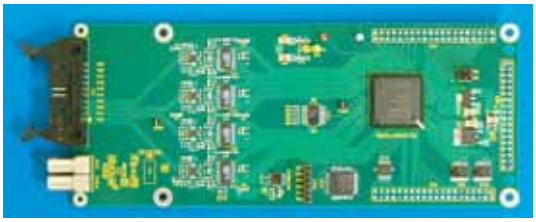

Figure 19: Flash ADC FINESSE card with 65 MHz sampling

potential sources such as the misalignment of tracking elements are regarded to be rather harmless since the correction based on the alignment calibration can be done accurately enough. Each correction is applied with an uncertainty of less than 10% of the correction values and the total systematic error by adding all the items can be made as small as 10^{-4}.

3.7 Data acquisition system

3.7.1 KEK-VME system at J-PARC

In E246 data taking was performed primarily using the standard TKO and FASTBUS system with some supplemental use of CAMAC system. The typical trigger rate was 200 Hz with a dead time of 10 to 15%. This was marginally tolerable, but a much faster system has to be employed in E06 (TREK). For example, the ADC has to have 100 times faster speed. Currently the KEK-VME system is being developed at KEK to support experiments like E06 (TREK) at J-PARC. KEK-VME [16] is based on the standard VME crate but it is equipped with a power supply for analog modules and digital signal nets for timing and trigger purposes. Readout modules are made as 9U type VME modules and called COPPER. This module has an on-board PC and four front-end card slots and can work with $\sim$10 kHz trigger rate.

3.7.2 Front-end cards and readout modules

Several A/D front-end cards which are called FINESSE are now available, and several developments are progressing in KEK. The 65 MHz sampling FADC with a 12-bit range has already been developed and they are ready for operation. This FADC will be used for the CsI(Tl) readout. A picture of the FADC card is shown in Fig.19. The charge to time converter (QTC) and pipeline TDC combination is a feasible candidate for counter and chamber read-out including the active polarimeter. The development of a pipeline TDC is progressing in the KEK electronics-system group. This TDC will be made with just a FPGA and counting a 1 GHz clock. The resolution of the TDC achieved is under 1 nano second. The picture of TDC card is shown in Fig.20. The research and developments of charge measurement using the ASIC technology are also progressing. QTC will be realized by this. A high-resolution TDC, a chip with under 30 ps resolution is now under development also using the ASIC technology. This developments are based on time memory cell (TMC) method. TMC used the internal delay of logic elements.

At a trigger rate of 10 kHz it is expected that the total dead time of DAQ should be less than 5%. Assuming an average detector ADC/TDC occuoancy of 5%, one event has

Figure 20: Pipeline TDC FINESSE card base on FPGA

Table 14: Readout channels and data size.

Detector element	Signal	Readout Device	Channel	Data size
CsI(Tl) calorimeter	768	Flash ADC	768	∼5 kB
Polarimeter	36,000	QTC+Pipeline TDC	3,000	∼400 B
MWPC (C2,C3,C4)	2,076	QTC+Pipeline TDC	248	∼160 B
GEM				
C0	1,164	QTC+Pipeline TDC	1,164	∼800 B
C1	11,340	QTC+Pipeline TDC	945	∼200 B
Target (MPPC)	432	QTC+Pipeline TDC	432	∼120 B
Counters, TOF	∼120	QTC+PL-TDC, HR-TDC	∼120	∼80 B
Total	∼52,000		∼6,680	∼6,7 kB

a data size of 6.7 kB and the total data flow at 10 kHz trigger is 67 MB/s, which is quite feasible to handle and to store. Readout performance is briefly summarized in Table 15

3.8 Other detector elements

In the new E06 (TREK) setup there will be also detector elements which are not upgraded substantially from E246 but will play important roles. They are described briefly here. Although there will be no essential change, small modifications of parameters are of course necessary to meet the new experimental conditions.

- **Beam Cherenkov counter:** Kaons in the beam are triggered by a Fitch-type Cherenkov counter [17] used in E246. The counter has two rings of PMTs for kaon multiplicity trigger and pion multiplicity trigger. Since the beam momentum now is 800 MeV/c instead of 660 MeV/c of E246, optics condition is different. Reflection

Table 15: Summary of readout performance

Parameter	Value	Condition
One event data size	6.7 kB	Assuming 5% data occupancy
Acceptable trigger rate	10,000 /s	Dead time of less than 5%
Data flow rate	67 MB/s	Trigger rate of 10 kHz

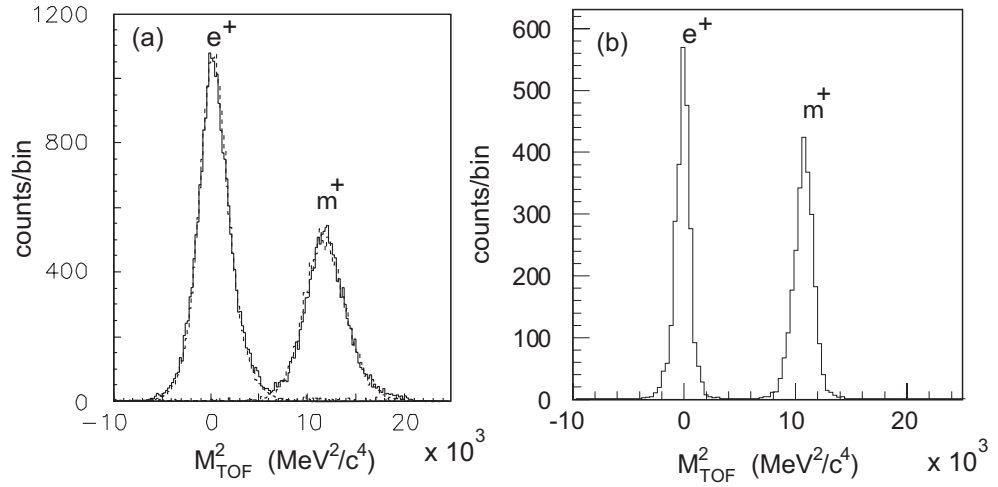

Figure 21: TOF mass spectra for the momentum range of 100 to 190 MeV/c for a) E246 (data) and b) E06 (simulation) assuming a timing resolution of $\sigma_t = 100$ ps. The separation of K_{e3} is now complete.

mirror angle as well as the radiator angle will be adjusted.

- **TOF counters:** The separation between $K_{\mu 3}$ μ^+ and background K_{e3} positrons is done by a TOF measurement between the start counter as the target shell (TOF1) and the TOF2 counter at the exit of the spectrometer. Because TOF1 was read by one side in E246, we had to be satisfied with the timing resolution of σ_t=270 ps. This can be improved to 100 ps by adopting a two-end reading method Fig.21.

- **Veto counters:** The introduction of the active polarimeter in E06 (TREK) reduces the necessity for veto-counters against the background particles into the polarimeter. In E246 the positron counters had to be protected for long (10 μs) time range from scattered particles from the beam region. It will be optional in E06.

4 K0.8 (K1.1BR) beamline

4.1 Stopped K^+ production at K1.1-BR

The basic concept of producing stopped K^+ at a low momentum separated kaon beamline with momentum of 0.8 GeV/c (K0.8) was presented in the proposal. The construction of a branch line of the K1.1 beamline as K0.8 was proposed and the beam optics design was also presented in the proposal, based on the calculation done by J.Doornbos in 2005 [18]. The following features were shown.

- In spite of the single stage electrostatic separator scheme, a fairly good K/π ratio can be anticipated due to the presence of a vertical focus IFY in front of EES. This situation is exactly same as in K1.8-BR as the branch of K1.8.

- A dispersion free horizontal focus HFOC after the third bend B3 plays an important role in removing the remaining contaminant pions.
- The channel acceptance of 6.0∼6.5 msr$\Delta p/p$% provides a K^+ beam with an intensity of $\sim 3 \times 10^6$/s at the primary beam intensity of 9μA at 30 GeV.

It was concluded that this beam with the predicted K^+ intensity with the $K/\pi > 2$ should be adequate for E06.

The grand floor plan of the phase-1 Hadron Hall, with the usage of the T1 target by K1.8 (+K1.8BR), K1.1 (+K1.1BR) and K0, was endorsed in the first PAC meeting. Therefore, we continued to pursue this K1.1BR scheme for the sopped K^+ beam. Meanwhile, the structure of the T1 target station and the vacuum vessel in direct downstream was also worked out and detailed drawings are now ready for fabrication. The optics design of 2005 is necessarily subject to changes due to the actual constrains in the front-end part according to the on-going real hardware designs.

4.2 Updated beam optics design

A new revised beam optics calculation has recently been performed taking into account all the modifications of the K1.1 upstream part parameters after the previous calculation [18]. The main changes are the drift distance from T1 to the first bend B1 which is now 2.0 m while it was 1.2 m before, and subsequent several distances. The detail of the calculation and the beam performance are shown in Ref.[19]. The main points are summarized as follows.

- The effective suppression of contaminant scatter and cloud pions by IFY and FHOC is not affected by the small changes of the channel parameters. A good K/π ratio is again predicted.
- The acceptance is, however, reduced to 4.5msr($\Delta p/p$ %) mainly due to the longer drift distance to B1.
- The muon contamination which was not treated in the previous calculation was checked and it was confirmed that it can be suppressed to an acceptable level at the final focus by closing HFOC.

The resultant main parameters of the beam are summarized in Table 16. The reduction of the channel acceptance is a crucial thing for the total design of E06. We will have to compensate for this by a longer beamtime than we have requested in the proposal.

There are several points yet to be finalized in conjunction with the main design of K1.1. The EES parameter used in the calculation (550 kV/11 cm gap and 2 m length) might be subject to change. For details, e.g., the cross section design of the beam duct is yet to be designed. However, we may regard that the basic features of the beam performance will not be much affected.

Regarding the real production of the beamline, there is no money assigned yet in the J-PARC construction budget. Detailed design of components has not yet been started, but we intend to use second-hand magnets as much as possible to suppress the construction cost. We await the start of J-PARC operation money. For the branch part, a contribution from an E06 (TREK) foreign group is also expected. As for the EES which becomes the most important element, we may apply the same design as the K1.8 first EES.

Table 16: Updated beamline performance of K0.8 as the branch of K1.1

Parameter	Value	Comment
Momentum	800 MeV/c	
Momentum bite	$\pm$2.5%	unchanged
Channel length	20.3 m	1.3 m longer
Channel acceptance	4.5 msr ($\Delta p/p$ %)	c.f. 4.6 msr ($\Delta p/p$ %) before
π^+/K^+ ratio	< 0.5	same as before
μ^+/K^+ ratio	< 0.5	new evaluation

5 Experimental Cost and Funding

5.1 Cost estimate

The cost estimate table of the proposal (Table 29) has been re-evaluated. It was 273,000 kYen for the detector elements, but this has now increased to 279,710 kYen due to more accurate estimate of the number of electronics channels. The breakdown is shown in Table 17.

The construction cost of the K1.1BR main part (the upstream part of K1.1) is not included in this summary, but this will cost 700-800 MYen including building up of the infrastructure such as cooling water capacity and electricity power. An effort to use recycled magnets may cut some fraction of this cost.

5.2 Funding

Since we submitted the proposal, the University of Saskatchewan's administration is providing a lot of support to the Canadian team in applying for the major grants, conference funds and in other ways. The American collaborators are also exploring their funding sources. Our collaborators also found monies to support students to engage in short-term R&D works and participate in collaboration meetings. A stage-2 approval from the J-PARC committee is highly desired, if not a pre-requisite, for the North American funding applications to be successful.

It is anticipated that KEK will assume responsibility of the transfer of the spectrometer system, as it will become a general J-PARC facility like SKS. Also, the installation of the K1.1 upstream section, a general purpose beamline of J-PARC, will be the responsibility of the J-PARC. The funding scenario for the E06 (TREK) experiment is summarized in Table 18. The Japanese group plans to apply for Grant-in-Aid support money.

6 Experimental Group and International Cooperation

6.1 Group member

The current collaboration members are listed in Table 19 not including students. At the present stage of approval we are still a relatively small group. However, because of our previous experience with E246, we have a large enough group to prepare and begin an

Table 17: Breakdown of cost estimate

Item	Cost (kYen)	Comment
K1.1BR branch part	50,000	B3, Q7, Q8, and HFOC including recycled ones
Transfer of spectrometer		
Magnet	25,000	Transport without disassembling
He cryogenics	157,000	CES from the company
Total	232,000	K1.1 upstream not included
Muon field magnet		
Magnets	30,000	12 sets
Support system	5,000	
Power supply	3,000	10 kW highly stabilized
Cooling system	2,000	piping etc.
Monitors	1,000	Hall instrument *etc.*
Active polarimeter		
Active stopper	36,000	12 sets
Amplifiers	6,000	
Assembly	3,000	
Gas system	3,000	E246 renewal
Target		
Fiber+connector	3,500	including clear fiber
MPPC	1,300	assuming 3kYen/ch at mass production
Amplifier+HV	3,200	including monitors
Assembly	12,000	support structure, MPPC panel etc.
Tracking		
C0 GEM chamber	11,000	assuming 1 U.S.$ = 100 Yen
C1 GEM chamber	16,900	assuming 1 U.S.$ = 100 Yen
Gas system	500	mainly piping
Support system	2,500	fine adjustment mechanism
CsI(Tl) readout		
APD	11,200	140$/channel
Amplifier etc.	10,000	incl. distributor, cables
Assembly	2,500	incl. APD gluing, module assembly
Monitors	500	incl. thermometers
Electronics and DAQ		
FADC	20,700	27 kYen/channel $\times$768 channels
QTC	33,400	5 kYen/channel, large uncertainty
Pipeline TDC	40,010	6 kYen/channel
Trigger + DAQ	5,000	
Field mapping		
Scanning device	12,500	incl. computer control
Instruments	2,500	Hall element etc.
Others	1,500	consumptions
Total of detector elements	279.710	the case of C1 installation
	(252,410)	the case of no C1 chamber

Table 18: Policy for funding

Item	Amount (kYen)	[Application to] or [budget source]
K1.1 upstream section	700,000-800,000	J-PARC operation money
K1.1BR branch part	50,000	Budget request in Canada incl. this cost
Transfer of spectrometer	182,000	KEK or J-PARC money
Target	some fraction	Fund application from a US university
Electronics	some fraction	Pool electronics for common use
Detector elements	about 270,000	Grant-in-Aid or J-PARC exp. money

experiment of this size. Of course we will make an effort further to attract additional collaborators. Noted that the foreign teams from Canada, US, and Russia are playing very active and important roles. We have also started a collaboration with Vietnam. The university faculty members in Canada and US will be able to attract graduate students in the future – once the beamtime schedule is established.

6.2 International cooperation

In the proposal we presented the framework of the international cooperation for TREK. This scheme has recently been confirmed in the collaboration meeting held in February 2007. Each constituent country is responsible for some parts of the detector elements. The responsibility distribution is shown in Table 20.

We hold group meetings regularly, once a year at KEK and once a year outside of Japan. The first meeting abroad was held in November, 2006 at MIT (USA), The next meeting will be held in Saskatoon (Canada) in August, 2007.

7 Safety issues

1) The Helium cryogenic system for the superconducting toroidal spectrometer will be operated under "The regulation of refrigeration rule of high-pressure gas safety law" in Japan. The system does not use any liquid N2 also at the magnet pre-cooling stage. Therefore, there is no concern about the strict high-pressure gas regulation in terms of "general gas".

2) The superconducting magnet excitation is not very strong. It is 0.9 T in the gaps and there is only small a leakage flux.

3) The wire-chamber gas is inflammable. In the normal operation of the chambers, the gas is recycling in a closed circuit and there is no loss. The purged gas will be guided to the outside of the building.

4) The high voltage for the scintillation counters and the chambers will be subject to standard safety procedures.

Table 19: E06 (TREK) experimental group

Country	Institution	Member
Canada	Univ of Saskatchewan (US)	C.Rangacharyulu[2)], R.E.Pywell, M.Bradley
	Univ of British Columbia /TRIUMF	M.Hasinoff, J.Doornbos, D.Gill, R.Henderson, P.Gumplinger
	U. Montreal (UM)	P.Depommier
U.S.A.	MIT	M.Kohl. R.Milner, B.Surrow, D.Hasell, J.Kelsey, M.Plesko, F.Simon
	Iowa State Univ.(ISU)	W.Anderson
	Univ of South Carolina (USC)	S.Strauch, C.Djalali
Russia	INR (Moscow)	A.Ivashkin[3)], A.Sadovsky, A.Kurepin
Vietnam	Nat.Sci.Univ in HCNC	D.P.Nguyen, C.V.Tao, T.Hoang
Japan	KEK	J.Imazato[1)], G.Y.Lim, Y.Igarashi, H.Nakayama, S.Sawada, H.Shimizu
	Osaka U.	S.Shimizu[4)], K.Horie
	Kyoto U.	T.Tsunemi
	Tohoku U.	H.Yamazaki
	Nat.Defnse Acad.	T.Matsumura

1) Spokesperson, 2) Foreign co-spokesperson, 3) Leader of Russian team, 4) Japanese group co-spokesperson

Table 20: International cooperation in E06 (TREK)

Country	Institutions	Responsibility	Base institute
Canada and U.S.A.	ISU, U.Saskatchewn, UBC/TRIUMF, USC	Target	TRIUMF shop
U.S.A.	MIT	GEM chambers	MIT
Russia	INR	CsI(Tl)	INR and KEK
Japan	Osaka U., KEK etc.	Polarimeter	KEK

References

[1] K. Paton *et al.*, "J-PARC E06" proposal, http://www-ps.kek.jp/e06/E06_proposal.pdf

[2] M. Abe *et al.*, Phys. Rev. D**73**, 072005 (2006).

[3] J. A. Macdonald, et al., Nucl. Instrum. Methods **A506**, 60 (2003).

[4] M. Aoki *et al.*, Phys. Rev. D**50**, 69 (1994).

[5] S. Kreitzman *et al.*, "Operation Manual for μSR at TRIUMF", http:// musr.org/howto/op/ musroprmanual.pdf, http:// musr.org/equip/lampf.html .

[6] R.D. Stambaugh *et al.*, Phys. Rev. Lett. **33**, 568 (1974); M. Senba, J. Phys. B: At. Mol. Opt. Phys. **31**, 5233 (1998).

[7] T. Ikeda *et al.*, Nucl. Instrum. and Methods **A401**, 243 (1997).

[8] D.V. Dementyev *et al.*, Nucl. Instrum. and Methods **A440**, 15 (2000).

[9] Hamamatsu Photonics K.K., Technical Information SD-28, Oct,2001; Cat.No. KAPD 1012J02, April, 2004.

[10] I. Britvitch *et al.*, Nucl. Instrum. and Methods **A535**, 523 (2004).

[11] T. Ikagawa *et al.*, Nucl. Instrum. and Methods **A538**, 640 (2005).

[12] "Second Workshop on Photo-sensors"(in Japanese), http://www-conf.kek.jp/rd-photon/.

[13] I. Britvicth, Y. Musienko, and D. Renker, Nucl. Instru. and Methods **A567**, 276 (2006).

[14] F. Simon *et al.*, to appear in the proceedings of the IEEE symposium on Nuclear Science and Medical Imaging (Sandiego, Oct,2006), http:// www-ps.kek.jp/ e06/mit/ieee2006.pdf.

[15] M. J. French *et al.*, Nucl. Instr. and Methods **A466**, 359 (2001).

[16] Y.Igarashi *et al.*, IEEE Trans Nucl. Sci. 52: 2866 (2005).

[17] M.P. Grigor'ev *et al.*, Instrum. Exp. Tech. **14**, 803 (1998).

[18] J. Doornbos, "An 800 MeV/c separated kaon beam at J-PARC", April 2005. http://trshare.triumf.ca/∼trjd/kstopbeam_jparc.pdf

[19] J. Doornbos, "Addendum to the report on the design of an 800 MeV/c separated kaon beam at J-PARC", May 2005. http://trshare.triumf.ca/∼trjd/koudolong.pdf

A Appendix : MC simulation of alignment calibration

A.1 Monte Carlo code

The purpose of Monte Carlo studies is to show the principal ability of a unique determination of the misalignments of the polarimeter using $K_{\mu 3}$ events when several misalignments are existing simultaneously, and its statistical accuracy. A simulation program based on a GEANT3 code was used. The 2mm thick stopper plates with 6mm gap (31 plates in total) and the muon holding field were installed in the existing E246/470 simulation program. The spin relaxation is discarded and the spin holding field is uniform 30 mT in the azimuthal direction. The stopper material is aluminum and no mechanical deformations were assumed. Although the muon stopping plate should be determined from an exact chamber analysis, we chose the plate here by following the muon track in the simulation. The e^+ direction was identified by the e^+ path in the adjacent gap of the muon stopped plate (the chamber efficiency is 100%).

In the real calibration measurement using data, we have to take into account the more detailed polarimeter structure and the positron detection characteristics with high enough statistical accuracy. However, the basic methodological performance of the calibration can be regarded to be proved in the present analysis. The muon field magnet design is now under way, and real field strength and its distribution might be slightly different. We regard 30 mT as the lowest value providing the safest result in the present study.

A.2 Global vs. local misalignment

There are two sorts of misalignments definition-wise in general: local ones and global ones. In the present analysis we would like to discuss only the global misalignment, which is the misalignment of the relevant detector elements as a whole. Considering the installation sequence of the detector that each detector element is assembled first with high precision and then the element is attached to the spectrometer as a unit, it is conceivable that the global alignment is more crucial. The local misalignment, on the other hand, corresponds to displacements of parts in each detector element from the ideal position due to limitation of mechanical assembling or machining. Their distribution can be regarded more or less statistical. Hence, the effects of local misalignment will be averaged out by integrating the events over the detector elements and it must be rather harmless.

In the case of the polarimeter, we can be more exact and define the global misalignment as the average value of misalignments from each part in the detector element with an appropriate weight such as the muon stopping density. For the misalignment parameter α for example,

$$\eta^{global} = \sum_{i=1}^{n} \omega_i \eta_i / \sum_{i=1}^{n} \omega_i \tag{12}$$

where α_i is the misalignment of each part and ω_i is the weight. As is shown next such global misalignment will induce a spurious left-right asymmetry which might mimic the true A_T, if no π^0 fwd/bwd cancellation is present. Thus, they should be primarily investigated. The effect from local distribution is higher order in general and it has a negligible correction, which was checked by a Monte Carlo calculation for each detector element.

A.3 Polarimeter structure and relevant global misalignments

Among the possible global misalignments of the three parallel displacements and three rotations: the parallel displacements should not play a role as long as the active stopper covers the whole muon stopping region because of parallel-shift symmetric structure. The rotation about the y-axis should not have an effect since it brings about only a rotation in the stopper planes. Hence, relevant global misalignments are:

- rotation of the active stopper around the r-axis: ϵ_r,
- rotation of the active stopper around the z-axis: ϵ_z.
- rotation of the muon field distribution around the r-axis: δ_r and
- rotation of the muon field distribution around the r-axis: δ_z.

A.4 Positron asymmetry due to misalignments

The outline of the calibration procedure were described in the proposal, which we repeat here in more detail. The asymmetry of the muon deacy positrons was calculated as

$$A = \frac{N_{fwd/left} - N_{bwd/right}}{N_{fwd/left} + N_{bwd/right}} \tag{13}$$

in the MC simulation for e^+ going in $fwd/back$ and $left/right$ directions under the condition of perfect alignment. The polarization was initially in the longitudinal direction lying in the median plane and precessing under the 30 mT field. The regions of fwd, bwd, $left$ and $right$ are defined appropriately. As is expected a precession pattern due to in-plane muon polarization is only observed in the e^+ fwd/bwd asymmetry.

When misalignments exist a small precession pattern appears in the e^+ $left/right$ asymmetry. More generally, for an arbitrary initial muon spin phase in the median planes θ_0, as shown in Fig. 17, The time dependent asymmetry, A, can be expressed as:

$$\begin{aligned} A(\omega t, \theta_0) &= \alpha_0\{(\epsilon_r - \delta_r)\cos(\omega t - \theta_0) + (\epsilon_z - \delta_z)\sin(\omega t - \theta_0) \\ &\quad +\delta_r\cos\theta_0 - \delta_z\sin\theta_0\} + \gamma \end{aligned} \tag{14}$$

Here we add an additional offset term γ due to possible asymmetric muon stopping distribution in the stopper or some unknown polarimeter defect such as chamber inefficiency. Rotation of the magnetic field generates the constant $\delta_r\cos\theta_0 - \delta_z\sin\theta_0$ term which mimics the actual T-violation effect and is rather crucial to ensure a precision of $\Delta P_T \sim 10^{-4}$.

The initial polarization was assumed to be P_l, completely parallel to the K^+ beam direction ($\theta_0 = 0$) in the simulation. Fig. 22 shows the precession oscillation pattern of the $left/right$ e^+ asymmetry with the finite misalignment of 1° rotation for one of the four ϵ_r, ϵ_z, δ_r, and δ_z misalignments by keeping other rotations to zero. The precession pattern with the form of $\epsilon_r\cos\omega t$, $\delta_r(1-\cos\omega t)$, $\epsilon_z\sin\omega t$, and $-\delta_z\sin\omega t$ are observed. In the precession pattern, the asymmetry coefficient α_0 and phases were determined. The fitted curvess are also shown.

A.5 θ_0 determination for $K_{\mu 3}$ events

The original muon spin direction was obtained from the kinematics of $K_{\mu 3}$ decay products with a form of [1]

$$\vec{A} = a_1(\xi) - a_2(\xi)[(m_K - E_\pi) + (E_\mu - m_\mu)(\vec{p}_\pi \cdot \vec{p}_\mu)/|\vec{p}_\mu|^2]\vec{p}_\mu \tag{15}$$

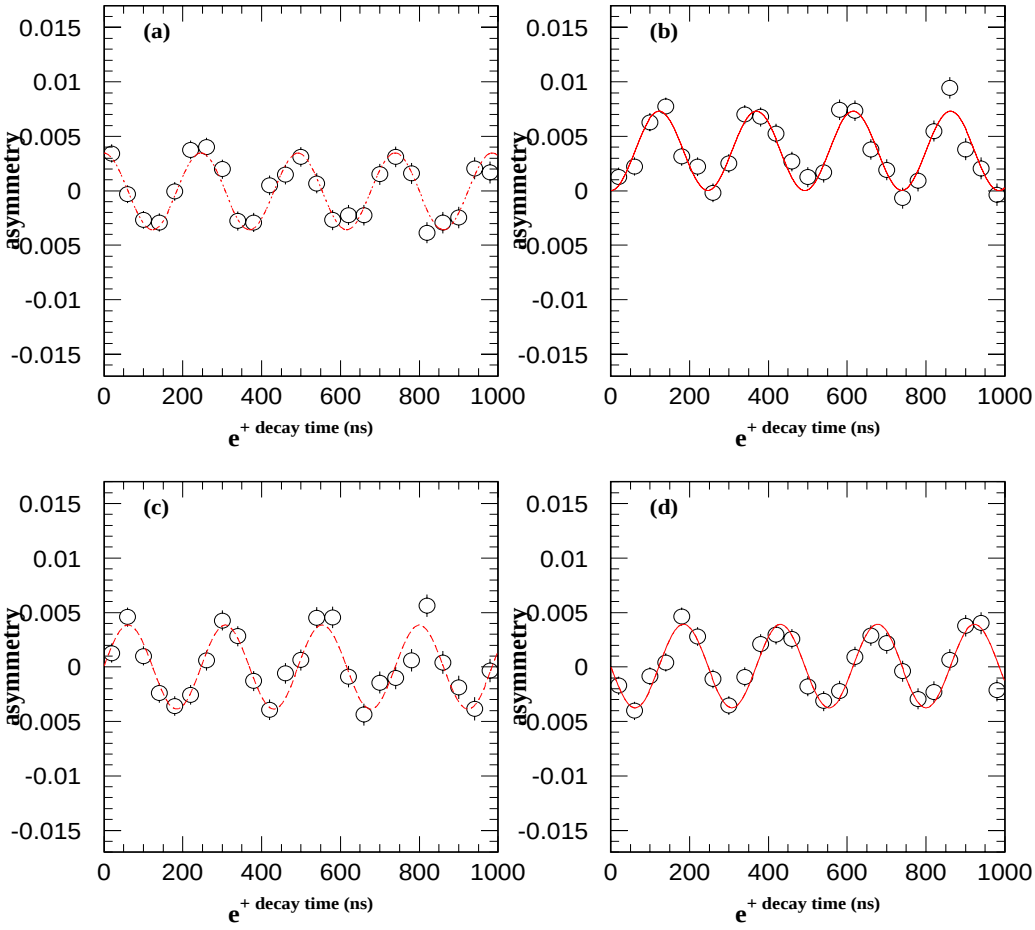

Figure 22: Left/right asymmetries with the finite misalignments of (a)δ_z, (b)δ_r, (c)ϵ_z, and (d)ϵ_r. One of four rotations was chosen by keeping other rotations to zero. Here, θ_0 was taken to be 0. Dotted lines are the fitted results. The precession pattern with the form of (a) $\epsilon_r \cos\omega t$, (b) $\delta_r(1-\cos\omega t)$, (c) $\epsilon_z \sin\omega t$, and (d) $-\delta_z \sin\omega t$ are observed.

$$-a_2(\xi)\vec{p}_\pi + m_K m_\mu \mathrm{Im}(\xi)(\vec{p}_\pi \times \vec{p}_\mu),$$

where

$$\begin{aligned} a_1(\xi) &= 2m_K^2[E_\nu + \mathrm{Re}(b(q^2))(E_\pi^* - E_\pi)], \\ a_2(\xi) &= m_K^2 + 2\mathrm{Re}(b(q^2))m_K E_\mu + |b(q^2)|^2 m_\mu^2, \\ b(q^2) &= 1/2[\xi(q^2) - 1], \\ E_\pi^* &= (m_K^2 + m_\pi^2 - m_\mu^2)/(2m_K). \end{aligned} \tag{16}$$

Here, the world average values of $K_{\mu 3}$ form factors reported by PDG were used. The θ_0 value of each $K_{\mu 3}$ decay at the muon stop position in the polarimeter was determined by taking into account the muon spin rotation by the spectrometer field. The muon spin direction was pursued in the simulation using the relativistic spin transportation method [2]. Here we neglected the spin rotation by the B field of the spin holding magnet during the muon transportation. Fig. 23 (a) shows the θ_0 distribution for $K_{\mu 3}$ events with the π^0 going forward (red) and backward (black) directions. Significant overlapping region can be seen in the figure.

A.6 Polarimeter misalignments

A Monte Carlo simulation was performed by assuming the misalignments of ($\delta_z = 5^\circ, \delta_r = 0^\circ$) and ($\delta_z = 0^\circ, \delta_r = 5^\circ$). The time-integrated e^+ $left/right$ asymmetries ($A(\theta_0)$) were obtained as a function of θ_0, using Eq.(8) as shown in Fig. 23 (c) and (d). Black and red circles are π^0 going forward and backward events, respectively. Here, a T-violation effect was not considered here ($\mathrm{Im}\xi = 0$). Since the $A(\theta_0)$ distribution due to these misalignments can be describe as $A(\theta_0) = \delta_r \cos\theta_0 - \delta_z \sin\theta_0 + \eta(\theta_0)$ which depends only on θ_0, the $A(\theta_0)$ distributions for events with π^0 going forward(A_{fwd}) and backward(A_{bwd}) should have the common θ_0 structure. These θ_0 dependences were successfully reproduced by the MC simulation, as shown in Fig. 23 (c),(d).

As well as the misalignment effects, the P_T extraction procedure was studied as follows. Assuming the finite $\mathrm{Im}\xi$, the MC simulation was performed with $\delta_r = \delta_z = 0$. Using the similar manner with the above misalignment studies, the e^+ left/right asymmetry was determined as a function of θ_0. Fig. 23 (b) shows the calculated $A(\theta_0)$ distributions, showing different θ_0 structure for π^0 going forward (black) and backward (red) events. The $A(\theta_0)$ values due to the forward and backward events have positive and negative values, respectively, in entire θ_0 region, while $A(\theta_0)$ from the misalignments have common θ_0 dependence. Therefore, δ and P_T can be individually determined by adding and subtracting A_{fwd} and A_{bwd} for each θ_0 bin.

$$A_{sum}(\theta_0) = (A_{fwd} + A_{bwd})/2, \tag{17}$$

$$A_{sub}(\theta_0) = (A_{fwd} - A_{bwd})/2. \tag{18}$$

A_{sub} and A_{sum} are π^0 fwd/bwd double ratio analysis and null asymmetry analysis, respectively for each θ_0 bin. The results of the MC simulation are shown in Fig. 18(a) for A_{sum} and Fig. 18 for A_{sub}, indicating good separation of P_T, δ_z, and δ_r. The P_T and δ values were obtained by making error weighted average over the entire θ_0 region (A_{sub}^{av}, A_{sum}^{av}).

Assuming the existence of both $\mathrm{Im}\xi$ and δ at the same time, the above A_{sum} and A_{sub} analyses were repeated in order to check the validity of this analysis scheme. Fig. 18 (a),(b)

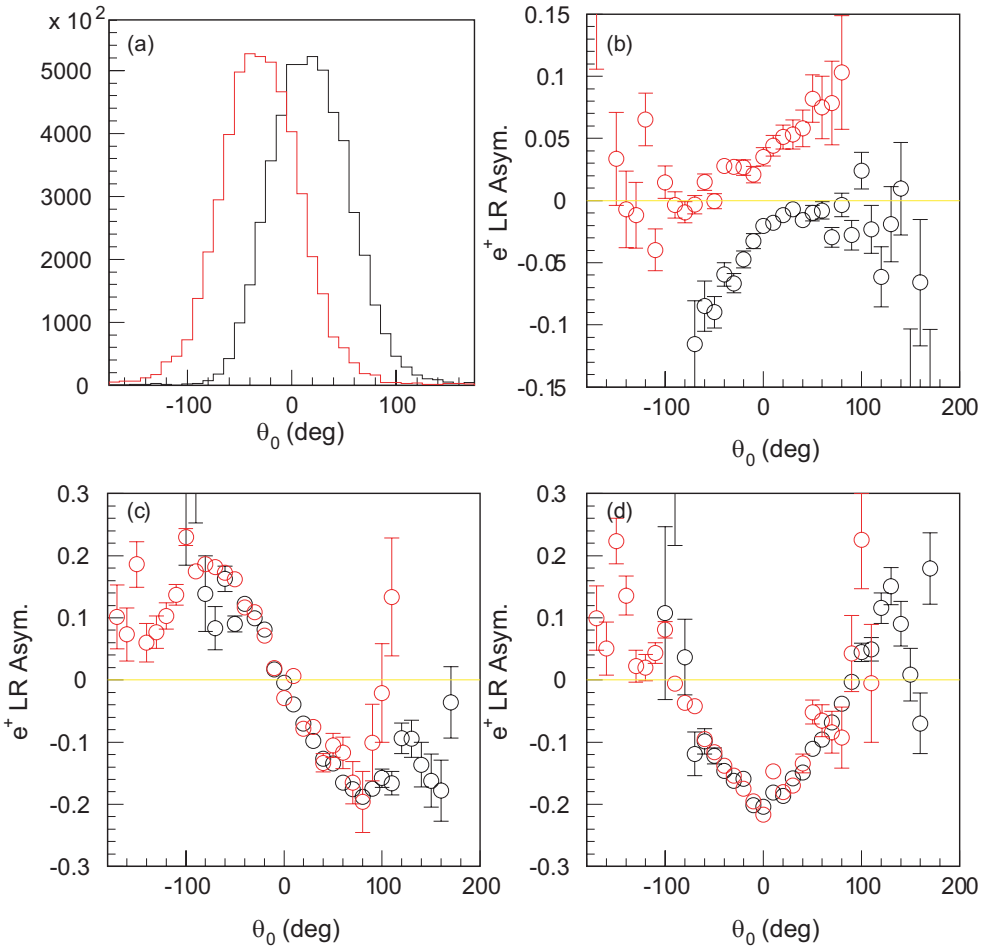

Figure 23: (a) $K_{\mu 3}$ θ_0 distributions and (b),(c),(d) e^+ $left/right$ asymmetries as a function of θ_0 for events with π^0 going forward (red) and backward (black). The asymmetries were obtained with the assumption of (b) pure P_T, (c) $\delta_z = 5°$ and (d) $\delta_r = 5°$. The $A(\theta)$ values due to π^0 forward and backward events have positive and negative values, while $A(\theta_0)$ from the misalignments have a common θ_0 dependence.

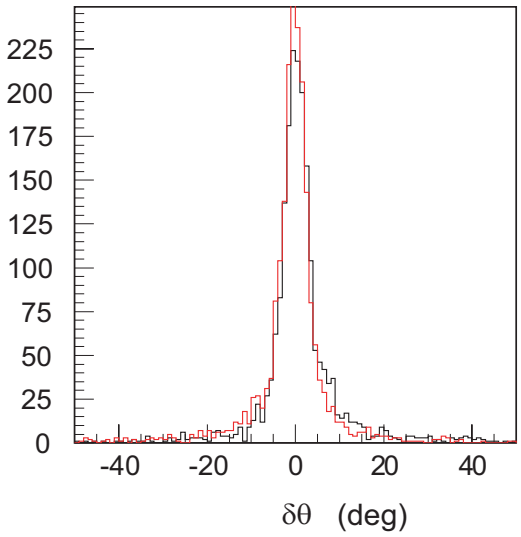

Figure 24: Distribution of θ_0 shift from its original value $\delta\theta$. θ_0 was calculated by using the observed μ^+ and π^0 information (black) and by changing $K_{\mu 3}$ form factors with $\pm 1\sigma$ level (red), and shifts from its original value were obtained. The θ_0 resolution was determined to be 2.3°(black) and 2.4°(red).

shows A_{sub} and A_{sum} distributions, respectively, corrected for the analyzing power of the polarimeter as, black circle: Im(ξ)=0.05, $\delta = 0$, blue circle: Im(ξ)=0.05, $\delta_z = 5°$, blue triangle: Im(ξ)=0.05, $\delta_r = 5°$, and red circle: Im(ξ)=0.05, $\delta_z = 5°$, $\delta_r = 5°$. Although they were obtained with various combinations of Imξ and δ, in any cases, the P_T and δ effects were successfully determined by the A_{sub} and A_{sum} analyses. The A_{sub}^{av} and A_{sum}^{av} values with the simultaneous existence of Imξ and δ were compared with those with single Imξ or δ cases, as shown in Fig. 18 (c),(d). They are consistent within errors, indicating the validity of the $A_{sub}(A_{sum})$ scheme to cancel out the misalignments (T-violation) and extract T-violation (misalignment) effect. Since P_T and δ contribute linearly to the e^+ $left/right$ asymmetry, the present analysis can provide good separation between them.

A.7 Ambiguity of θ_0

Here we used correct θ_0 values obtained by substituting true μ^+ and π^0 information into Eq.(16), however uncertainties from (a) finite detector resolutions and (b) error of $K_{\mu 3}$ form factors should degrade the asymmetry distributions in the actual analysis. To study the θ_0 uncertainty, θ_0 was calculated by using the observed μ^+ and π^0 information for (a) and by changing the $K_{\mu 3}$ form factors with $\pm 1\sigma$ level for (b). The distribution of θ_0 shift from its original value is shown in Fig. 24. Black and red histograms are for (a) and (b), respectively. The θ_0 resolutions were determined to be 2.4° from RMS values containing the tail part. Although these finite resolution have to be taken into account for the actual A_{sub} and A_{sum} analyses, the asymmetry distributions will not be strongly affected by this uncertainty and the systematic error due to this effect is less important.

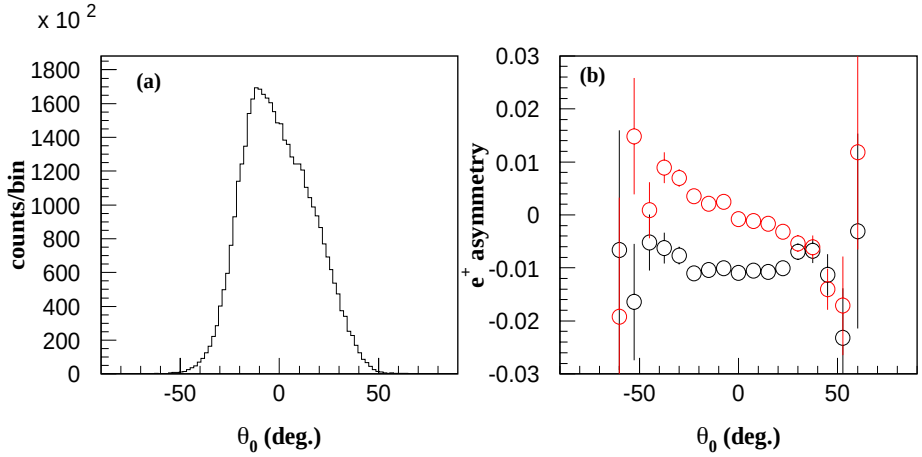

Figure 25: (a) θ_0 distribution of the $K_{\mu 2}$ events and (b) their time integrated asymmetry of as a function of θ_0 for the case of the finite δ_z (red circles) and δ_r (black circles) terms. The $K_{\mu 2}$ events are concentrated around $\theta_0 = 0$ and are sensitive to δ_r.

A.8 Redundant measurement of alignments using $K_{\mu 2}$ and $K_{\pi 2}$ events

Since measurement of the misalignments is essential for the T-violation search in $K_{\mu 3}$, a redundant measurement other than $K_{\mu 3}$ events is highly desirable. In order to do that, we utilized the longitudinal polarization of $K_{\mu 2}$ (events with $\theta_0 \sim 0$) and the muon polarization from decay-in-flight π^+ of $K_{\pi 2}$ decays (events with $\theta_0 \sim -\pi/2$ or $\sim \pi/2$) (See the proposal [1]).

The former and the latter are sensitive to δ_r and δ_z, respectively. The transverse decay of pion in the CM system with a muon emitted in the gap median plate produces a polarization component of stopped muons in the radial direction. Radial and longitudinal components of $K_{\mu 2}$ muon polarization are also available to determined the misalignments.

In order to improve the reliability of the alignment measurement, the polarization calibration should be performed using both in-flight $K_{\pi 2}$ muons and $K_{\mu 2}$ muons independently and compared with the results obtained using $K_{\mu 3}$ events. Since it is possible to determine θ_0 for both $K_{\mu 2}$ and $K_{\pi 2}$ decays, the time integrated e^+ asymmetry can be obtained as a function of θ_0. Fig. 25 (a),(b) show the θ_0 distribution of the simulated $K_{\mu 2}$ events and their left/right asymmetries, respectively. The sin and cos oscillation patterns in the asymmetries corresponding to δ_z and δ_r were observed, which should be consistent with the $K_{\mu 3}$ results. Thus, the systematic check by this measurement of misalignments using $K_{\mu 2}$ and $K_{\pi 2}$ decays will play an important role to strengthen the reliablility of alignments.

References

[1] N.Cabibbo and A. Maksymowicz, Phys. Lett. **9**, 352 (1964).

[2] P. Depommier, KEK-E246 Technical Note No.28 (Internal).

B Appendix : Production of GEM chambers

B.1 C0 cylindrical chamber

An increasing number of projects have considered using GEM technology for cylindrical tracking chambers with curved foils. One chamber (TACTIC) has been designed at TRIUMF, for the measurement of heavy charged recoil fragments in nuclear astrophysics experiments [1]. TACTIC is a ionization chamber with a single GEM layer for charge amplification and segmented single anode strip readout. The BoNuS experiment at the Thomas Jefferson National Accelerator Facility recently used a GEM-based radial time projection chamber (RTPC) in a solenoidal magnetic field along with the CLAS/Hall B detector, to tag energetic neutrons in quasi-elastic deuteron electro-disintegration by measuring spectator protons at very low momenta [2]. The BoNuS RTPC is a cylindrical triple-GEM chamber with 2D pad readout. The large drift volume of the RTCP enables full reconstruction of the curved tracks in the solenoidal field through radial time projection. Although this detector has been used to track heavily ionizing low-energy protons, it is in principle capable of measuring minimum ionizing particles. At CERN, a cylindrical triple-GEM chamber is being developed as a vertex tracker for the follow-up of the NA49 experiment [3]. This chamber consists of two half shells with a radius of 10 cm using 30 cm x 30 cm GEM foils of the COMPASS type. The most complex example of a cylindrical GEM chamber is a GEM-based vertex tracker in cylindrical shape consisting of five triple-GEM shells developed for an upgrade of the KLOE detector at DAPHNE [5]. The five triple-GEM plus readout shells (20 layers) are seamless and are equipped with 2D-readout with spiraling strips intersecting in two helicities.

In contrast to the above examples of BoNuS and TACTIC, the proposed C0 GEM chamber has to be capable of efficient detection of minimum ionizing tracks. The absence of a magnetic field in the target region keeps the tracks very straight and in radial direction, hence only the (z, ϕ) coordinates of the trajectory crossing through the cylinder surface at a certain radius are of interest. Subsequently, the drift volume can be kept small, which is beneficial for the resulting position and timing resolution of the device.

Like the KLOE chamber, the cylinder will cover the full 2π azimuthal acceptance without blind regions. As such, the individual foil layers will be glued seamlessly to individual cylinders with defined radii that are assembled later in the process. The readout strips need to be two-dimensional with readout electronics at the end-caps only. The two layers of spiraling strips of the KLOE chamber are given by one dedicated readout layer at ground potential and by the bottom side of the last GEM layer which is at a finite voltage. There are several disadvantages of such a design. The readout is no longer decoupled from the amplification process, and any discharge may impact the readout electronics. Also, the required charge sharing between the two readout layers depends delicately on the choice of the right voltage of the last step between the bottom layer of the last GEM and the ground potential of the second readout layer.

The 2D readout design of the TREK C0 chamber will employ a slightly different technique. The active part of the readout foil should be produced like the planar case of COMPASS (or the MIT prototype), i.e. a rectangular pattern with longitudinal and transverse strips. When wound up to a cylinder, the longitudinal strips will be along z and the transverse strips oriented along the azimuthal direction of the cylinder. The starting point is 50 μm Kapton with 5 μm Cu cladding on both sides. Strips in one orientation will first

be chemically etched on one side. This side will be glued bottom-down onto a carrier foil (100 μm glass fiber in case of COMPASS, but this can be thinner, e.g. 50 μm Kapton). Then the other side is chemically etched for the strips in the cross orientation. Finally, laser etching is used to remove the Kapton that is now still covering the first strip layer that was glued onto the carrier foil. Now both strip layers are exposed to the same surface to collect the amplified charge.

The azimuthal length of the readout foil should be twice the cylinder circumference, i.e. $2 \times 2\pi R$ allowing for two windings of the cylinder. The first winding, i.e. the first half of the foil has the strip pattern described before and covers the active part on the inner surface. The second winding would only extend the azimuthal strips to guide them to the end-cap of the cylinder. The strip pattern of this "guide layer" could be made such that all strip extensions are of the same length. The required additional material of that second wind would essentially be only 50 μm Kapton plus the etched signal lines on one side, i.e. with little contribution to the material budget. The downstream end of the readout layer will host the APV25 front-end chips. Flexible circuit boards will be used to connect the front-end chips with the control unit to read out all strips of both layers at the downstream end. In order to minimize materials within the CsI(Tl) calorimeter, the length of the readout layer in the longitudinal direction will exceed the active length of the cylinder, to guide the signals to the APV25 chips further downstream outside of the calorimeter. Such a strip extension is easily possible as the primary length of readout strips can be up to 5 m.

With the same pitch of 635 μm as the COMPASS chamber a resolution of 50-70 μm can be established. The readout at the downstream cylinder end-cap will be using flexible transient circuit boards to transport and bundle the signal channels to planar circuit boards hosting the readout electronics. With an active length of 30 cm and a radius of 7 cm, the readout of the proposed C0 element will consist of a total of 30 cm / 635 μm + $2\pi \times 10$ cm / 635 μm $\simeq$ 470 + 1000 $\simeq$ 1200 channels.

B.2 C1 planar chamber

A prerequisite for mass production of triple-GEM tracking detectors is the availability of GEM foils. So far, the only source for these devices has been the CERN-EST-DEM photo-lithographic workshop. However, their capacity is limited and unable to meet the increasing worldwide demand for GEM foils. To address this problem a collaboration with the Plymouth, MA based company Tech-Etch, Inc. has been formed and a SBIR proposal (Small Business Innovation Research) has been approved in 2006. The goal of the proposal by Tech-Etch in collaboration with BNL, MIT and Yale is to develop the technology at Tech-Etch for commercial production of GEM foils which meet the requirements for use in nuclear and particle physics and astrophysics research besides long-term medical imaging and homeland security applications. GEM foils now are routinely produced by Tech-Etch. Recently, a comprehensive test experiment with three triple-GEM prototype detectors built with GEM foils produced by Tech-Etch was performed at the Meson Test Beam Facility at Fermilab.

In parallel, research and development will be done to develop a low mass detector prototype that can be used in beam tests which meets the requirements of a minimized material budget both for the STAR Forward GEM Tracker (FGT) arrangement and the C1 tracking element in the TREK experiment. While the C1 element and the GEM trackers for STAR are both planar detectors that have many of the required properties in common,

Table 21: Cost estimate for the cylindrical C0 triple-GEM detector.

Item	Amount	k$	Remarks
GEM chamber mechanics	4	10	$2500/chamber
GEM foils	30	6	$200/GEM foil
Readout foils	10	2	$200/foil
Readout layer R&D		5	
Hybrids	60	6	$100/flexible circuit board
Hybrid R&D		5	
APV25 chips	60	1.5	$25/chip
Cables		3	Signal and HV
FEE	7680	1.5	$2/channel, in house R&D
Integration FEE/DAQ		20	
Power supply		10	HV pods
Gas system		10	part of common system for C0+C1
Mechanical support		20	in house R&D
Misc. items		10	
Total		110	No contingency

the development of the C0 chamber will significantly extend the R&D activities at the MIT GEM lab.

B.3 R&D timeline, cost and manpower

The availability and fabrication of GEM foils by Tech-Etch has made excellent progress. Several planar GEM prototypes are existing and working well which was recently demonstrated in a dedicated test experiment at Fermilab. During this year, a light planar prototype applicable to both the STAR and J-PARC planar detector layout will be designed and built. The detailed design and construction of a prototype C0 chamber is envisioned to be started in 2008. The studies on the cylindrical prototype C0 chamber will be pursued in parallel with the development of the low mass planar element. The design and construction of the final C0 and C1 chambers are envisioned for 2009-2010. Tables 21 and 22 list the expected cost to develop and manufacture the C0 and C1 elements.

For the C1 chambers, we propose to build 14 final detectors (two acting as spares), and at least two prototypes.

The available manpower of the GEM R&D group at MIT consists of Professor Dr. Richard Milner (Principal Investigator), Assistant-Professor Dr. Bernd Surrow (Group leader GEM R&D), Principal Research Scientist Dr. Douglas Hasell, Research Scientist Dr. Michael Kohl, Mechanical Engineer Jim Kelsey, Electronic Engineer Dr. Miro Plesko, Postdoctoral Associate Dr. Frank Simon, and students.

References

[1] http://tactic.triumf.ca/

Table 22: Cost estimate for the C1 GEM detector based on 12 planar triple-GEM chambers.

Item	Amount	k$	Remarks
GEM chamber mechanics	16	8	$500/chamber
GEM foils	50	10	$200/GEM foil
Readout foils	20	4	$200/foil
Readout layer R&D		5	
Hybrids	144	14	$100/flexible circuit board
Hybrid R&D		5	
APV25 chips	144	3.5	$25/chip
Cables		12	Signal and HV
FEE	18432	37	$2/channel, in house R&D
Integration FEE/DAQ		20	
Power Supply		10	HV pods
Gas system		10	part of common system for C0+C1
Mechanical support		20	in house R&D
Misc. items		10	
Total		169	No contingency

[2] http://www.jlab.org/%7Ehcf/bonus/

[3] http://gdd.web.cern.ch/GDD/

[4] M.C. Altunbas *et al.*, "Construction, test and commissioning of the triple-GEM tracking detector for COMPASS", Nucl. Instr. and Meth. **A490** (2002) 177

[5] http://www.lnf.infn.it/lnfadmin/direzione/roadmap/LoIKLOE.pdf